



**COMPUTATIONAL MODELING OF THE DIELECTRIC BARRIER
DISCHARGE (DBD) DEVICE FOR AERONAUTICAL APPLICATIONS**

THESIS

Christopher S. Charles, 1st Lieutenant, USAF

AFIT/GAP/ENP/06-02

**DEPARTMENT OF THE AIR FORCE
AIR UNIVERSITY**

AIR FORCE INSTITUTE OF TECHNOLOGY

Wright-Patterson Air Force Base, Ohio

APPROVED FOR PUBLIC RELEASE; DISTRIBUTION UNLIMITED

The views expressed in this thesis are those of the author and do not reflect the official policy or position of the United States Air Force, Department of Defense, or the United States Government.

AFIT/GAP/ENP/06-02

**COMPUTATIONAL MODELING OF THE DIELECTRIC BARRIER
DISCHARGE (DBD) DEVICE FOR AERONAUTICAL APPLICATIONS**

THESIS

Presented to the Faculty

Department of Engineering Physics

Graduate School of Engineering and Management

Air Force Institute of Technology

Air University

Air Education and Training Command

In Partial Fulfillment of the Requirements for the
Degree of Master of Science (Applied Physics)

Christopher S. Charles, BS

1st Lieutenant, USAF

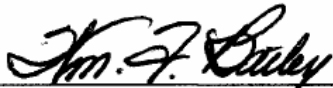
June 2006

APPROVED FOR PUBLIC RELEASE; DISTRIBUTION UNLIMITED

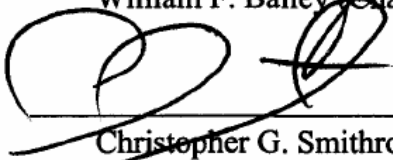
**COMPUTATIONAL MODELING OF THE DIELECTRIC BARRIER
DISCHARGE (DBD) DEVICE FOR AERONAUTICAL APPLICATIONS**

Christopher S. Charles, BS
1st Lieutenant, USAF

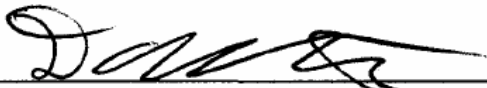
Approved:



William F. Bailey (Chairman)



Christopher G. Smithro (Member)



David E. Weeks (Member)

12 May 2006
date

12 May 06
date

12 May 06
date

Abstract

Dielectric Barrier Discharge (DBD) type devices, when used as plasma actuators, have shown significant promise for use in many aeronautical applications. Experimentally, DBD actuator devices have been shown to induce motion in initially still air, and to cause re-attachment of air flow over a wing surface at a high angle of attack. This thesis explores the numerical simulation of the DBD device in both a 1D and 2D environment. Using well established fluid equation techniques, along with the appropriate approximations for the regime under which these devices will be operating, computational results for various conditions and geometries are explored. In order to validate the code, results are compared to analytic or experimental data whenever possible, or matched with other similar numeric simulations to help establish the accuracy of the code. Solutions to Poisson's equation for the potential, electron and ion continuity equations, and the electron energy equation are solved semi-implicitly in a sequential manner. Each of the governing equations is solved by casting them onto a tridiagonal grid, and using the computationally efficient Thomas algorithm to solve 1D regions in a single iteration. The Scharfetter-Gummel flux discretization method is used to add stability to the code when transitioning from a field to diffusion dominated region or vice versa. Estimates for the ionization and recombination rates and for the transport coefficients of the background gas are calculated as a function of the local average electron energy, and updated for every calculation point in the domain on the completion of the solution to the electron energy equation. Results are then recorded and used as a

starting point for the next time step. The basis for the 2D geometry relies heavily on its 1D counterpart, but with the inclusion of a Gauss-Seidel line iterative method to solve Poisson's equation, and a superposition method for keeping track of ion, electron, and electron energy fluxes. Appropriate boundary conditions are implemented to close the computational region at the boundaries, take into account any space charge present in the computational area, and keep track of surface charge buildup on any dielectric surfaces if present. In the 2D geometry, momentum transfer to the background gas could be estimated by tracking the charge particle movement and their interactions with the neutral background gas; and the effects of various electrode placements, driving potentials, and driving frequencies (if an AC potential source is present) could be used to further the understanding of DBD operation. Results from the 1D and 2D code are presented, as well as limitations of the current work and proposed future refinements.

Acknowledgments

I would like to express my sincere appreciation to my advisor, Dr. Bailey, for his guidance, support, and patience; and the rest of the very helpful AFIT physics professors. My time here was enlightening, as well as educational.

Thank you to my family, I appreciate your love and support. You give me joy.

Thank you to everyone else for the preparation.

Christopher S. Charles

Table of Contents

	Page
Abstract	iv
Acknowledgments	vi
List of Figures	viii
List of Tables	x
I. Introduction	1
Background and Importance of the Dielectric Barrier Discharge	1
DBD Device Configuration	3
II. Computational Modeling	6
Introduction	6
Moments of the Boltzmann Equation	6
Discretization of Equations and the Scharfetter-Gummel technique	11
Boundary Conditions	17
BOLSIG Fits for Rate and Transport Coefficients	19
III. Computational Set-up and Potential Solver	30
1D Computational Set-up	30
2D Computational Set-up	37
IV. Results and Conclusions	45
DC Discharge Sheath Test	45
Ambipolar Diffusion	50
Constant Characteristic Parameters Comparison	53
1D Fixes	57
2D Results and Problems	60
V. Summary of Work and Recommendations for Future Efforts	66
Summary of Work	66
Recommendations for Future Efforts	66
Bibliography	70
Vita	72

List of Figures

Figure	Page
1. DBD device configuration for aeronautical application (8:1).	1
2. Boundary layer flow re-attachment caused by a DBD device (17:2124).	2
3. Charge build-up on a DBD dielectric under AC operating conditions (7:2).	4
4. Various geometrical arrangements for the DBD device (14:1820).	5
5. Plot of F_1 and F_2 as functions of Z	14
6. Computational fit for the electron mobility as a function of average energy.	21
7. Computational fit for the k_L coefficient as a function of average energy.	21
8. Set-up for the DBD device as described by Eq (47).	27
9. Line method used for solving the 2D potential profile.	28
10. Characteristic set-up geometry for the 1D numeric model.	30
11. Potential profile for 1D region with no dielectrics or free charge.	31
12. Potential profile for inserted dielectric and no free charge.	32
13. Potential profile for no dielectrics and positive free charge.	33
14. Potential profile for inserted dielectrics with free charge.	35
15. Semi-implicit algorithm for solving the governing equations.	36
16. Characteristic set-up geometry for the 2D numeric model.	37
17. 2D potential profile and associated E field vectors for no free charge.	40
18. 2D potential profile and associated E field vectors for negative surface charge.	40
19. The 2D potential solver results for a pseudo 1D geometry.	43
20. 5-point averaging Excel and numeric code results for similar regions.	44
21. Potential profile during formation of the DC discharge sheath in a system with bare electrodes.	47
22. Normalized electron density during formation of the DC discharge sheath in a system with bare electrodes.	47
23. Normalized ion density during formation of the DC discharge sheath in a system with bare electrodes.	47
24. Potential profile during formation of the DC discharge sheath in a system with dielectrics coatings.	49
25. Normalized electron density during formation of the DC discharge sheath in a system with dielectric coatings.	49
26. Normalized ion density during formation of the DC discharge sheath in a system with dielectric coatings.	49

Figure	Page
27. DC discharge results reported by Hilbun (12:11).....	50
28. Electron density during ambipolar diffusion.	51
29. Ion density during ambipolar diffusion.	51
30. Potential profile during ambipolar diffusion.	52
31. Charge distribution after 1 μs for constant characteristics comparison.....	56
32. Charge distribution after 3 μs for constant characteristics comparison.....	56
33. Magnified view of the instabilities near the anode encountered at P=10 Torr.	57
34. BOLSIG fits for relating the reduced field to the local average electron energy.	59
35. Gaussian used as an initial condition for charge density distribution.....	61
36. Plots of the 2D potential profile progression for various times. Changes in the profile are seen as charge moves in the system and accumulates on the dielectric surface.	63
37. Electron number density for various times after initial Gaussian. Instabilities around the exposed electrode area are seen.....	64
38. Charge buildup on the dielectric surface at end of simulation. The region between 7 and 17 units on the axis is the location of the exposed electrode. Therefore, no charge was allowed to accumulate there.	65
39. Induction of flow over electrodes with various potentials phasing (17:2125).....	67
40. Pentadiagonal matrix for implicit potential solution.	68

List of Tables

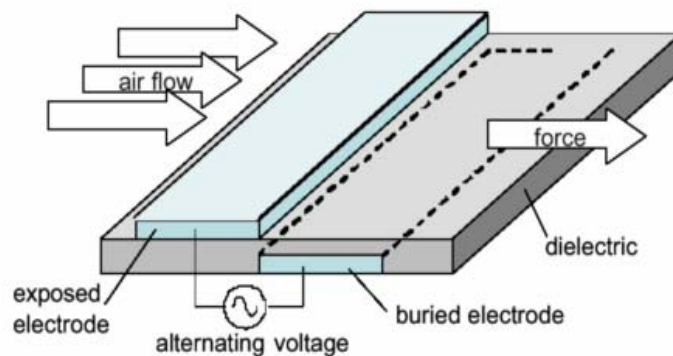
Table	Page
1. Computational values for the electric field converging on the analytic solution.	42
2. List of calculated accumulation of surface charge on the dielectric surfaces for various times during ambipolar diffusion.....	53
3. Values used for comparison between constant characteristic systems.	54

COMPUTATIONAL MODELING OF THE DIELECTRIC BARRIER DISCHARGE (DBD) DEVICE FOR AERONAUTICAL APPLICATIONS

I. Introduction

Background and Importance of the Dielectric Barrier Discharge

The Dielectric Barrier Discharge (DBD) device has been put to use since 1857 when Werner von Siemens used to produce ozone at atmospheric pressures from the oxygen in air. Today, DBD devices are still in use as ozone generators, but have found many more uses in industry, science, and military applications. Such uses include plasma television displays, pumps for CO₂ lasers, toxic gas decomposition for pollution control, and the modification of air flow over a surface (14:1819). The Fig 1 shows the nominal flow control set-up for the DBD device as described by Font et al (8:1).



Plasma actuator configuration.

Figure 1. DBD device configuration for aeronautical application (8:1).

This technology is of particular interest to the United States military, specifically the Air Force, to improve the effectiveness of their aircraft and weapon systems. DBD devices have been shown to induce air flow over a surface, reattach flow to an airfoil at high angles of attack, such as shown in Fig 2; and show promise of eventually replacing flaps and ailerons on aircraft (DBD devices are commonly called plasma actuators when referring to flow control). By eliminating the hydraulics on aircraft and replacing them with electrical wires, plasma actuators would open the door to building stronger, lighter, more robust airfoils, with faster maneuvering response time and fewer moving parts to malfunction. This is especially advantageous when considering Unmanned Combat Aerial Vehicles (UCAVs), and pushing the performance envelope above and beyond what human physiology can withstand.

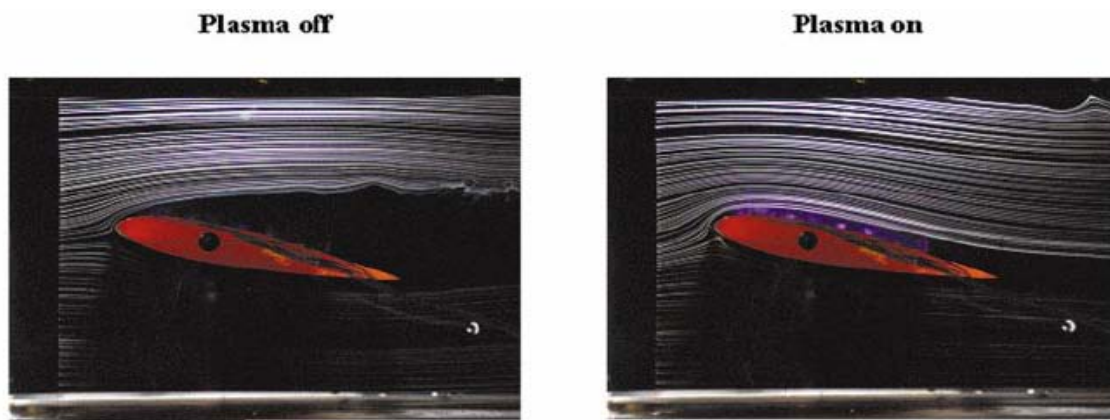


Figure 2. Boundary layer flow re-attachment caused by a DBD device (17:2124).

The maturation of DBD actuator technology by the United States represents the next generation of design enhancements that will continue to keep Air Force jets flying higher, faster, and farther with the potential of being stronger, lighter, and more highly maneuverable. The development of robust and accurate computational code for

simulating the outcome of these ongoing experiments would represent a great step toward understanding their behavior more completely. Replacing the experimental configurations that need to be built and tested in a laboratory with a numeric simulation, would result in great saving in time and resources, and could possibly lead to faster development. In short, an effective and efficient numerical code would help mature and deploy the DBD actuator technology more quickly than traditional methods and also result in a significant costs savings to the Air Force.

The focus of this thesis will be to provide a greater understanding of the discharge dynamics, through observing momentum and energy transfer in the plasma using fluid dynamics and computational methods. Eventually, the availability of accurate modeling software that is grounded in theory will allow engineers, once left with only trial and error, to optimize their designs in a cost effective way. A robust and accurate computational tool would help predict the energy and momentum imparted to the surrounding airflow via the DBD actuator for different device configurations and operating parameters. This will provide the Air Force with a low cost, quick turn around, effective way of designing their next generation of aerial vehicles.

DBD Device Configuration

A DBD device can be made from any configuration of electrodes, separated by a dielectric barrier, operated under an alternating current (AC) configuration, as opposed to direct current (DC). The devices are commonly used in the glow discharge region of the plasma spectrum, where the number density of positively and negatively charge species

are roughly equivalent, and a neutral gas many orders of magnitude greater in density is present. This background pressure can range from a few Torr to 1 Atmosphere (ATM) (20:8). Initially, the applied potential difference on the electrodes must be great enough to initiate gas breakdown. While operation is possible for a short time using a DC potential, the discharge will eventually extinguish due to a buildup of charge on the dielectric barrier as notionally seen in Fig 3. This buildup effectively reduces the applied potential across the gap between the electrodes and the discharge is extinguished. This buildup may play a crucial role in the continued operation and characterization of these devices under AC operating conditions. It might act to *seed* the ionization of the neutral gas on the reverse cycle of the potential as shown below in Fig 3. This *seeding* could in fact be the mechanism by which an asymmetric force on the neutral flow is coupled to the background gas during operation (9:9). For this project, the charge will be considered trapped on the dielectric surface and only secondary emission from exposed electrode surfaces due to ion impact will be characterized.

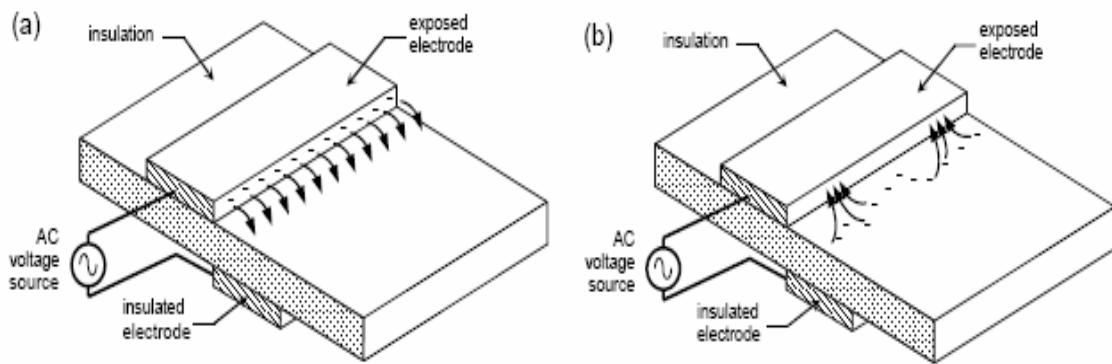


Figure 3. Charge build-up on a DBD dielectric under AC operating conditions (7:2).

The dielectric barrier can be either an insulating coating on the anode or cathode of the device, or a layer of insulating material placed somewhere in between. A variety of DBD configurations exist, some of which are shown in Fig 4. These various arrangements stem from the multiple uses of DBD type devices for industrial applications, plasma T.V. display light generation, and aeronautical flow control purposes. It should be noted that while these DBD devices have found widespread usage in the modern world because of their proven operational capability, the physics behind their operation and plasma dynamics involved are not well understood. Therefore, this thesis will focus on characterizing the mechanisms involved in DBD operations through the use of macroscopic fluid equations. The numeric simulation will be done for both 1D and 2D geometries.

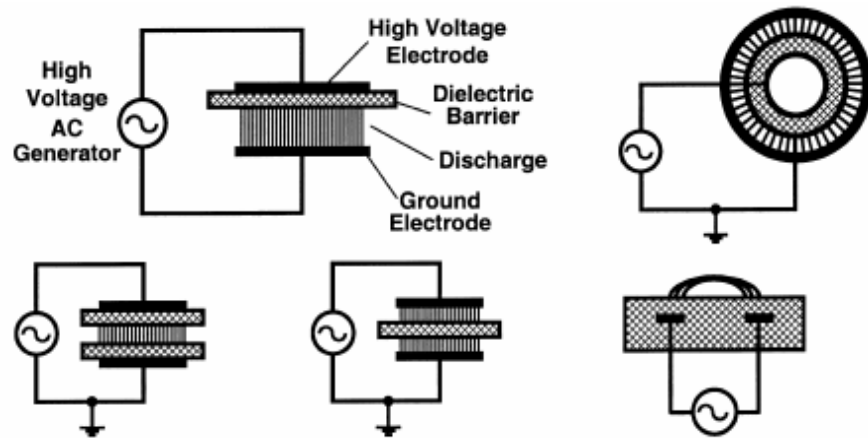


Figure 4. Various geometrical arrangements for the DBD device (14:1820).

II. Computational Modeling

Introduction

Tracking the position of all the individual particles in the DBD system, as well as their ancillary velocity vectors for any system with more than a few constituents is problematic, if not impossible. Of course, the only exact solution is to track each constituent on a microscopic scale; however, memory requirements, as well as computational time limitations force an approximate solution where only the macroscopic parameters of the system are accounted for and varied. In making a few physically reasonable approximations, the fluid equations governing the DBD system can be derived from the Boltzmann equation, allowing for numeric modeling of different conditions and configurations in a reasonable amount of time without losing too much information about the physical reality of the model. For this thesis, macroscopic fluid type equations will be used to track the location and movement of the electrons and positively charged ions in the system, as well as the average local electron energy density at each spatially discretized location.

Moments of the Boltzmann Equation

The Boltzmann equation is defined by:

$$B_{\text{boltzmann}} \equiv \frac{\partial f}{\partial t} + \vec{v} \cdot \vec{\nabla} f + \vec{a} \cdot \vec{\nabla}_{\vec{v}} f = \left(\frac{\delta f}{\delta t} \right)_{\text{collision}}. \quad (1)$$

This equation represents the temporal evolution of the distribution function, f , (or the probability of finding a plasma species with a particular position and velocity (\vec{v})). The

first term represents the change in the distribution function over time; this is ultimately what will be solved for to give a solution over all time to a system given some set of initial conditions. The second term describes how the distribution changes in space, or configuration coordinates, as the particles move through the system with a certain velocity and direction. The third shows how the species distribution is changing due to external forces acting to accelerate the charged particles. And finally, the term on the right hand side represents collisional interactions among the plasma species as time passes, such as ionization and recombination, and how these affect the total distribution of the system. The zeroeth and second *moments* of the Boltzmann equation, are defined by:

$$Moment_0 \equiv \int B_{boltzmann} d\vec{v} \quad (2)$$

and

$$Moment_2 \equiv \int B_{boltzmann} \frac{1}{2} m^s \vec{v} \vec{v} d\vec{v} \quad (3)$$

respectively. The integrals are done over all space with respect to the velocity coordinates. These two *moments*, along with the solution to the first *moment*, also called the momentum equation, which will be approximated using the Scharfetter-Gummel flux discretization technique described later, can be solved to yield the continuity and energy equations for a particular species, with m designating the mass of the species. The species (designated by a superscript s) included in this thesis will be limited to singly positively charged ions and electrons only. A brief development of the continuity

equation will be looked at next, but results for the energy equation will only be stated. Full derivations can be found in almost any introductory plasma physics course text (6:19-26).

By simplifying each term of the zeroeth *moment* of the Boltzmann equation defined above, the continuity equation can be shown to develop as follows (19):

$$\int \left(\frac{\partial f}{\partial t} + \vec{v} \cdot \vec{\nabla} f + \vec{a} \cdot \vec{\nabla}_v f = \left(\frac{\delta f}{\delta t} \right)_{\text{collision}} \right) d\vec{v} = \underbrace{\int \frac{\partial f}{\partial t} d\vec{v}}_{\text{Term 1}} + \underbrace{\int \vec{v} \cdot \vec{\nabla} f d\vec{v}}_{\text{Term 2}} + \underbrace{\int \vec{a} \cdot \vec{\nabla}_v f d\vec{v}}_{\text{Term 3}} = \underbrace{\int \left(\frac{\delta f}{\delta t} \right)_{\text{collision}} d\vec{v}}_{\text{Term 4}} \quad (4)$$

Term 1 reduces to:

$$\int d\vec{v} \frac{\partial f}{\partial t} = \frac{\partial}{\partial t} \int f d\vec{v} = \frac{\partial n}{\partial t} \quad (5)$$

because $n = \int f d\vec{v}$, is the number density of the species.

Term 2 reduces to:

$$\int \vec{v} \cdot \vec{\nabla} f d\vec{v} = \int f d\vec{v} \vec{\nabla} \cdot \vec{v} = \vec{\nabla} \cdot \int f d\vec{v} \vec{v} = \vec{\nabla} \cdot n\vec{v} = \vec{\nabla} \cdot \vec{\Gamma} \quad (6)$$

recognizing that the number density times the velocity is defined as the species flux ($\vec{\Gamma}$) into or out of any particular volume element.

Term 3 reduces to:

$$\int \vec{a} \cdot \vec{\nabla}_{\vec{v}} f d\vec{v} = \int \vec{\nabla}_{\vec{v}} \cdot \vec{a} f d\vec{v} = \int_{Surface} \vec{a} \cdot \hat{n} f dS = 0 \quad (7)$$

by using the divergence theorem, and recognizing that any distribution goes to zero as the surface used in the integral approaches infinity.

Finally, term 4 reduces to:

$$\int \left(\frac{\delta f}{\delta t} \right)_{collisional} d\vec{v} = \int d\vec{v} \left(\frac{\delta f}{\delta t} \right)_{collisional} = \left(\frac{\delta n}{\delta t} \right)_{collisional} = S - L \quad (8)$$

resulting in a source and loss term determined by the collisional interaction of the particles in the system.

The resulting continuity equation can be rewritten from Eq (4) as:

$$\frac{\partial n}{\partial t} + \vec{\nabla} \cdot \vec{\Gamma} = S - L. \quad (9)$$

If ionization and recombination of the positively charged ions and electrons are the only source and loss terms considered for this project, then the $S - L$ term above can be rewritten as:

$$S - L = \nu n^e - \beta n^e n^i \quad (10)$$

with ν representing the electron impact ionization frequency on the neutral gas, and the recombination coefficient represented by β . The local temporal change of the number

density and the divergence of the flux in 1D, along the X-axis in this case, can be recast in a finite difference form as:

$$\frac{\partial n}{\partial t} = \frac{n^{s,t} - n^{s,t-1}}{\Delta t} \quad (11)$$

and

$$\vec{\nabla} \cdot \vec{\Gamma} = \frac{\partial}{\partial x} \cdot \vec{\Gamma} = \frac{\vec{\Gamma}_{right} - \vec{\Gamma}_{left}}{\Delta x} \quad (12)$$

respectively. The superscript t refers to a specific point in time. The divergence term reduction above is commonly referred to as a *three-point* formula, even though the third point does not appear in the equation (4:171-172). This 1D discretization is appropriate for this project since particle fluxes into or out of a local volume will only be considered along one specific axis at a time. Note that the flux characters retain their vector quality, even when reduced to 1D in the example above; this indicates the ability of the flux to be directed in either a positive or negative sense.

Finally, all terms from the previous development can be combined to yield the 1D continuity equation for this project:

$$\frac{n^{s,t} - n^{s,t-1}}{\Delta t} + \frac{\vec{\Gamma}_{right}^{s,t} - \vec{\Gamma}_{left}^{s,t}}{\Delta x} = \nu n^{e,t-1} - \beta n^{e,t-1} n^{i,t-1}. \quad (13)$$

The electron energy equation takes on a similar form:

$$\frac{n^{e,t} u^{e,t} - n^{e,t-1} u^{e,t-1}}{\Delta t} + \frac{5}{3} \frac{\vec{\Gamma}_{right}^{n^e u^e, t} - \vec{\Gamma}_{left}^{n^e u^e, t}}{\Delta x} = -q \vec{\Gamma}^{e,t} \cdot \vec{E} - N k_L n^{e,t-1} . \quad (14)$$

$n^e u^e$ designates the electron energy density. The first term on the right hand side is a source due to Joule heating, with q as the unsigned charge on an electron; and the second term is a collisional power loss associated with electron-neutral collisions. If the units of energy are specified to be in eV instead of the S.I. unit of Joules, then the q in Eq (14) above is divided out in the conversion, and everything else remains the same. Neutral number density is determined by specifying the pressure (P) at which the simulation will be running, and converting via:

$$N = \frac{P}{k_b T} , \quad (15)$$

with T as the temperature of the system and k_b as Boltzmann's constant.

Discretization of Equations and the Scharfetter-Gummel technique

With the fluid equations specified, the next step is to approximately describe them for the discrete points in space that make up the computational domain. In a 2D geometry, but considering only the change in density due to movement of the species along the X-axis in this example, the electron and ion continuity equations can be written as:

$$\frac{n_{x,y}^{s,t} - n_{x,y}^{s,t-1}}{\Delta t} + \frac{\vec{\Gamma}_{x+\frac{1}{2},y}^{s,t} - \vec{\Gamma}_{x-\frac{1}{2},y}^{s,t}}{\Delta x} = \nu n_{x,y}^{e,t-1} - \beta n_{x,y}^{e,t-1} n_{x,y}^{i,t-1} . \quad (16)$$

While the electron energy equation can be written as:

$$\frac{n_{x,y}^{e,t} u_{x,y}^{e,t} - n_{x,y}^{e,t-1} u_{x,y}^{e,t-1}}{\Delta t} + \frac{5}{3} \frac{\vec{\Gamma}_{x+\frac{1}{2},y}^{n^e u^e,t} - \vec{\Gamma}_{x-\frac{1}{2},y}^{n^e u^e,t}}{\Delta x} = -\vec{\Gamma}_{x,y}^{e,t} \cdot \vec{E}_{x,y} - N k_L n_{x,y}^{e,t-1}. \quad (17)$$

with the subscripts now designating a particular position in 2D space. This project will set the distance between evaluation points to be equal, that is $\Delta x = \Delta y$. The final form of these equations suggests that for given initial conditions the evolution of the charged species densities and energy density can be solved for any later time in a sequential manner. Solving then for the current time step, these two equations can be rewritten as:

$$n_{x,y}^{s,t} = (S_{x,y}^{s,t} - L_{x,y}^{s,t} - \frac{\vec{\Gamma}_{x+\frac{1}{2},y}^{s,t} - \vec{\Gamma}_{x-\frac{1}{2},y}^{s,t}}{\Delta x}) \Delta t + n_{x,y}^{s,t-1} \quad (18)$$

and

$$n_{x,y}^{e,t} u_{x,y}^{e,t} = (S_{x,y}^{n^e u^e,t} - L_{x,y}^{n^e u^e,t} - \frac{5}{3} \frac{\vec{\Gamma}_{x+\frac{1}{2},y}^{n^e u^e,t} - \vec{\Gamma}_{x-\frac{1}{2},y}^{n^e u^e,t}}{\Delta x}) \Delta t + n_{x,y}^{e,t-1} u_{x,y}^{e,t-1}. \quad (19)$$

Having described the source and loss terms earlier, the flux terms in the above equations will now be described using the Scharfetter-Gummel flux discretization scheme. This flux, which appears in both the continuity and energy equations, is obtained from the solution of the first *moment* of Boltzmann's equation by applying the drift and diffusion approximation (12:3). By using this flux description for the continuity and energy equations, computational stability is added to the model, allowing for relatively coarser grid point spacing. This is a result of the ability of the Scharfetter-

Gummel technique to smooth the transition between field driven and diffusion dominated regions (12:4). This smoothness is achieved by the built-in ability of the flux representation to account for the direction of the electric field at any given point (*up-winding*), relate information about the species densities on either side of that point, and appropriately weight the contributions of each term when describing the flux into or out of the point. The *up-winding* effect of the Scharfetter-Gummel technique is not easily seen at first, and a more in-depth example describing the behavior under limiting conditions can be found in the work by Hilbun (13:9-10). The flux terms for the continuity equations are:

$$\vec{\Gamma}_{x+\frac{1}{2},y}^{s,t} = \left(\frac{n_{x,y}^{s,t} D_{x,y}^{s,t-1} \exp(Z_{x+\frac{1}{2},y}^{s,t}) - n_{x+1,y}^{s,t} D_{x+1,y}^{s,t-1}}{\Delta x} \right) \left(\frac{Z_{x+\frac{1}{2},y}^{s,t}}{\exp(Z_{x+\frac{1}{2},y}^{s,t}) - 1} \right) \quad (20)$$

and

$$\vec{\Gamma}_{x-\frac{1}{2},y}^{s,t} = \left(\frac{n_{x-1,y}^{s,t} D_{x-1,y}^{s,t-1} \exp(Z_{x-\frac{1}{2},y}^{s,t}) - n_{x,y}^{s,t} D_{x,y}^{s,t-1}}{\Delta x} \right) \left(\frac{Z_{x-\frac{1}{2},y}^{s,t}}{\exp(Z_{x-\frac{1}{2},y}^{s,t}) - 1} \right). \quad (21)$$

Where the Z terms are defined as:

$$Z_{x+\frac{1}{2},y}^{s,t} = -\text{sign}[s] \frac{\mu_{x+\frac{1}{2},y}^{s,t-1}}{D_{x+\frac{1}{2},y}^{s,t-1}} (\phi_{x+1,y} - \phi_{x,y}) \quad (22)$$

and

$$Z_{x-\frac{1}{2},y}^{s,t} = -\text{sign}[s] \frac{\mu_{x-\frac{1}{2},y}^{s,t-1}}{D_{x-\frac{1}{2},y}^{s,t-1}} (\phi_{x,y} - \phi_{x-1,y}) \quad (23)$$

with $sign[s]$ taking the value of +1 for the positive ions and -1 for electrons. The ϕ 's represent the scalar potential at a given grid point, and D and μ are the diffusion and mobility coefficients respectively. Special limiting *if* statements were included in the computational code, to account for regions where the change in potential was very small or zero, or where the change was very large. This kept the F terms defined below from returning as undefined, or as a number greater than the computer could handle due to the exponential factors in the terms of Eq (24). It should be noted that the values of Z , D , and μ for the electron energy flux are the same as those appearing in the electron continuity equation (i.e. $Z_{x,y}^{n^e u^e, t-1} = Z_{x,y}^{e, t-1}$, $D_{x,y}^{n^e u^e, t-1} = D_{x,y}^{e, t-1}$, $\mu_{x,y}^{n^e u^e, t-1} = \mu_{x,y}^{e, t-1}$). To further reduce the equations into a more manageable form, the $F1$ and $F2$ terms:

$$\begin{aligned} F1[Z] &= \frac{Z \exp(Z)}{\exp(Z) - 1} \\ F2[Z] &= \frac{Z}{\exp(Z) - 1} \end{aligned} \quad (24)$$

are introduced. Shown in the figure below is a plot of these two F functions.

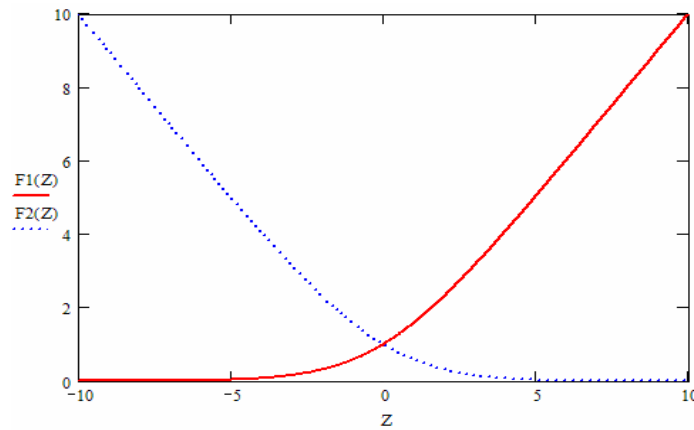


Figure 5. Plot of F1 and F2 as functions of Z.

The limit of the F functions for small Z's in the range of $\pm 10^{-7}$ about zero was set to 1 based on L'Hopital's rule, while the limit for the Z's that were greater than 150 or less than -150 was set equal to Z and 0 for F1 and F2 respectively. After a little algebra, new forms for the flux terms can be shown reduced as:

$$\bar{\Gamma}_{x+\frac{1}{2},y}^{s,t} = \frac{n_{x,y}^{s,t} D_{x,y}^{s,t-1} F1[Z_{x+\frac{1}{2},y}^{s,t}] - n_{x+1,y}^{s,t} D_{x+1,y}^{s,t-1} F2[Z_{x+\frac{1}{2},y}^{s,t}]}{\Delta x} \quad (25)$$

and

$$\bar{\Gamma}_{x-\frac{1}{2},y}^{s,t} = \frac{n_{x-1,y}^{s,t} D_{x-1,y}^{s,t-1} F1[Z_{x-\frac{1}{2},y}^{s,t}] - n_{x,y}^{s,t} D_{x,y}^{s,t-1} F2[Z_{x-\frac{1}{2},y}^{s,t}]}{\Delta x}. \quad (26)$$

Finally, substitutions for the previously determined representations for source and loss can be made. The final form of the electron continuity equations in 1D along the X-axis reduces to:

$$\begin{aligned} & n_{x-1,y}^{e,t} \left(-D_{x-1,y}^{e,t-1} F1[Z_{x-\frac{1}{2},y}^{e,t}] \Delta t \right) + \\ & n_{x,y}^{e,t} \left((\Delta x)^2 + D_{x,y}^{e,t-1} F1[Z_{x+\frac{1}{2},y}^{e,t}] \Delta t + D_{x,y}^{e,t-1} F2[Z_{x-\frac{1}{2},y}^{e,t}] \Delta t \right) + \\ & n_{x+1,y}^{e,t} \left(-D_{x+1,y}^{e,t-1} F2[Z_{x+\frac{1}{2},y}^{e,t}] \Delta t \right) = \quad . \quad (27) \\ & n_{x,y}^{e,t-1} \left((\Delta x)^2 + \frac{1}{2} \nu_{x,y} n_{x,y}^{i,t-1} \Delta t (\Delta x)^2 - \frac{1}{2} \beta n_{x,y}^{i,t-1} \Delta t (\Delta x)^2 \right) \end{aligned}$$

The ion continuity equations in 1D along the X-axis can be re-written as:

$$\begin{aligned}
& n_{x-1,y}^{i,t} \left(-D_{x-1,y}^{i,t-1} F1[Z_{x-\frac{1}{2},y}^{i,t}] \Delta t \right) + \\
& n_{x,y}^{i,t} \left((\Delta x)^2 + D_{x,y}^{i,t-1} F1[Z_{x+\frac{1}{2},y}^{i,t}] \Delta t + D_{x,y}^{i,t-1} F2[Z_{x-\frac{1}{2},y}^{i,t}] \Delta t \right) + \\
& n_{x+1,y}^{i,t} \left(-D_{x+1,y}^{i,t-1} F2[Z_{x+\frac{1}{2},y}^{i,t}] \Delta t \right) = \\
& n_{x,y}^{i,t-1} \left((\Delta x)^2 + \frac{1}{2} \nu_{x,y} n_{x,y}^{e,t-1} \Delta t (\Delta x)^2 - \frac{1}{2} \beta n_{x,y}^{e,t-1} \Delta t (\Delta x)^2 \right)
\end{aligned} \tag{28}$$

where the source and loss terms for this project will always depend on the previous values of the electron and ion densities to ensure generation or recombination of the charged species occurs in pairs, making the numeric code is stable, and not allowing any inequality between production and loss. In a similar manner, the electron energy equation in 1D along the X-axis takes on the final form:

$$\begin{aligned}
& n_{x-1,y}^{e,t} u_{x-1,y}^{e,t} \left(-\frac{5}{3} D_{x-1,y}^{e,t-1} F1[Z_{x-\frac{1}{2},y}^{e,t}] \Delta t \right) + \\
& n_{x,y}^{e,t} u_{x,y}^{e,t} \left((\Delta x)^2 + \frac{5}{3} D_{x,y}^{e,t-1} F1[Z_{x+\frac{1}{2},y}^{e,t}] \Delta t + \frac{5}{3} D_{x,y}^{e,t-1} F2[Z_{x-\frac{1}{2},y}^{e,t}] \Delta t \right) + \\
& n_{x+1,y}^{e,t} u_{x+1,y}^{e,t} \left(-\frac{5}{3} D_{x+1,y}^{e,t-1} F2[Z_{x+\frac{1}{2},y}^{e,t}] \Delta t \right) = \\
& n_{x,y}^{e,t-1} u_{x,y}^{e,t-1} \left((\Delta x)^2 \right) - (\vec{\Gamma}_{x,y}^e \cdot \vec{E}_{x,y}) \Delta t (\Delta x)^2 - \frac{1}{2} n_{x,y}^{e,t-1} k_L N \Delta t (\Delta x)^2
\end{aligned} \tag{29}$$

where the electron flux term, $\vec{\Gamma}_{x,y}^e$, at the grid point is the average of the electron flux at the current time step of the closest mid-points which is solved for during the solution of the electron continuity equation using the Scharfetter-Gummel discretization technique. These flux values are determined when the electron continuity equation is solved. It should be recognized that the values of the electron flux and electric field in the energy

equation retain their vector nature, indicating that they lie along a particular axis in 2D space. The factor of $\frac{1}{2}$ multiplying the source or loss terms in all the governing equations is a manifestation of calculating the source or loss for each volume element in 2D space as a superposition of both 1D elements along the two possible axes. This will be elaborated on more in Chapter 3.

With the three governing equations now reduced into a compact tridiagonal form, the evolution of the ion and electron densities and the electron energy from some initial condition can now be found, given that appropriate values for the boundary conditions of the system and the existing unknowns can be determined.

Boundary Conditions

Since the Scharfetter-Gummel flux representation depends on neighboring points to determine intermediate values, and this model will assume that the space charge density at any surface boundaries is zero, realistic conditions for the fluxes at these boundaries need to be defined (2:1379).

The flux of the electrons at a surface boundary will be defined as:

$$\vec{\Gamma}_{boundary}^{e,t} = \pm \frac{1}{4} n_{adjacent}^{e,t} v_{adjacent}^{e thermal,t} \mp \gamma \vec{\Gamma}_{adjacent}^{i,t-1} \quad (30)$$

where the plus or minus terms indicates that the thermal flux term is always directed towards the surface boundary, and that the secondary emission is directed away from the boundary. γ represents the secondary emission coefficient for positive ion impact onto the

surface of any exposed electrode. γ will be set to 0.02 for this project. $v_{adjacent}^{e\,thermal,t}$ is the value of the thermal velocity of the electrons at the point next to the boundary, expressed in terms of the average electron energy at that point:

$$v_{adjacent}^{e\,thermal,t} = 4.19 \times 10^5 \sqrt{u_{adjacent}^{e,t-1}} . \quad (31)$$

The average electron energy, u^e , is found by dividing the energy density in the solution of the energy equation, by the number density in the solution of the electron continuity equation.

The conditions for the ion flux at the surface boundaries are somewhat different, but still give a realistic value over the time scale used because of their much slower response to any applied fields and relatively cooler temperature when compared to the electrons. That being said, the movement of the ions is modeled as field driven only at the surface boundaries using the Scharfetter-Gummel technique. To satisfy the condition of having only field driven flux, the diffusion dependency of the technique must be zeroed. This is done by temporarily setting the ion density at the surface boundary equal to its adjacent grid point. One final *if* statement must be incorporated however. The boundary flux must only exist if the electric field is also directed toward the boundary. This condition keeps ions from moving out of the region that was temporarily assigned a value to zero the diffusion term, but is otherwise modeled as having no charge density. The final form of the ion flux at the surface boundary, which can be integrated into the previously determined ion continuity equations, is:

$$\vec{\Gamma}_{adjacent}^{i,t} = \frac{(F1[Z_{adjacent\pm\frac{1}{2}}^{i,t}] - F2[Z_{adjacent\pm\frac{1}{2}}^{i,t}])n_{adjacent}^{i,t}D_{adjacent}^{i,t-1}}{\Delta x} \quad (32)$$

where the \pm term in the Z factor indicates if an adjacent grid point is either to the left or the right of the surface boundary in this X-axis example.

Finally, the electron energy flux into the surface boundary takes on a form very similar to that of the electron flux. It is modeled as:

$$\vec{\Gamma}_{boundary}^{n^e u^e, t} = \pm \frac{1}{3} n_{adjacent}^{e,t} u_{adjacent}^{e,t} v_{adjacent}^{e thermal, t}. \quad (33)$$

Any electron energy flux out of the boundary, due to secondary emission, is accounted for in the Joule heating term of the energy equation.

Conditions for non-surface boundaries, for the 2D geometry, are implemented by using *ghost* cells around the computational domain that have the same value for densities as their neighboring cells, and where the perpendicular component of the electric field has been defined to be zero, so as not to allow any loss in the system. While the zeroing of the perpendicular component of the electric field at the non-surface boundary is not a physical reality, it is a good approximation if the size of the domain and distance of the boundary is far enough away from the active region of the simulation (11:40).

BOLSIG Fits for Rate and Transport Coefficients

With the boundary conditions adequately defined, the values of the transport parameters and kinetic rate coefficients in the continuity and energy equations will now

be defined. The values of β, γ , and $\mu_{x,y}^{i,t}$ or $D_{x,y}^{i,t}$ are assumed to be constants that were measured experimentally given the material make-up of the system, the type of gas in the system, and the pressure of the gas in the system. Using the Einstein relation to define a relationship between $\mu_{x,y}^{i,t}$ and $D_{x,y}^{i,t}$, for the positively charged ions in the system, it can be shown that:

$$\frac{D_{x,y}^{i,t}}{\mu_{x,y}^{i,t}} = \frac{k_b T}{q}. \quad (34)$$

Approximating room temperature for this simulation leaves a value of about 1/40 for the right hand side of the equation, showing that if one parameter value is known from an experimental result, the other can be easily determined.

The values of $\mu_{x,y}^{e,t}, D_{x,y}^{e,t}, \nu_{x,y}$, and k_L as a function of local average electron energy can be determined by using the BOLSIG Boltzmann equation solver. This excellent freeware tool has proven reliable and accurate, as well as easy to use. Curve fits of the unknown coefficients as a function of average electron energy can be obtained for specified gases and mixtures of gases, as well as their dependence on ambient pressure. This project uses the BOLSIG results for a pure atmosphere of either Ar or N₂. Two representative plots of the numerical results from BOLSIG, as well as their associated fits are shown below in Fig 6 and Fig 7 (3).

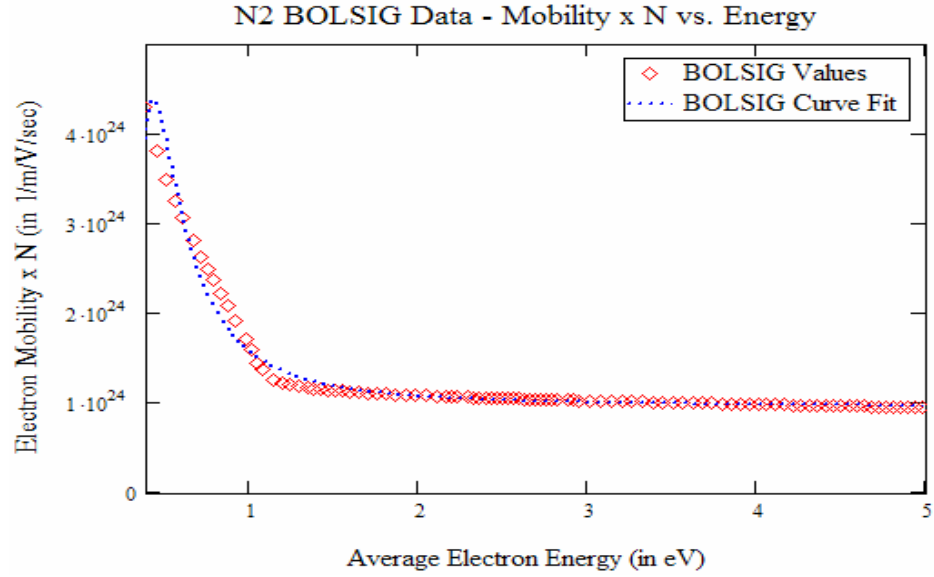


Figure 6. Computational fit for the electron mobility as a function of average energy.

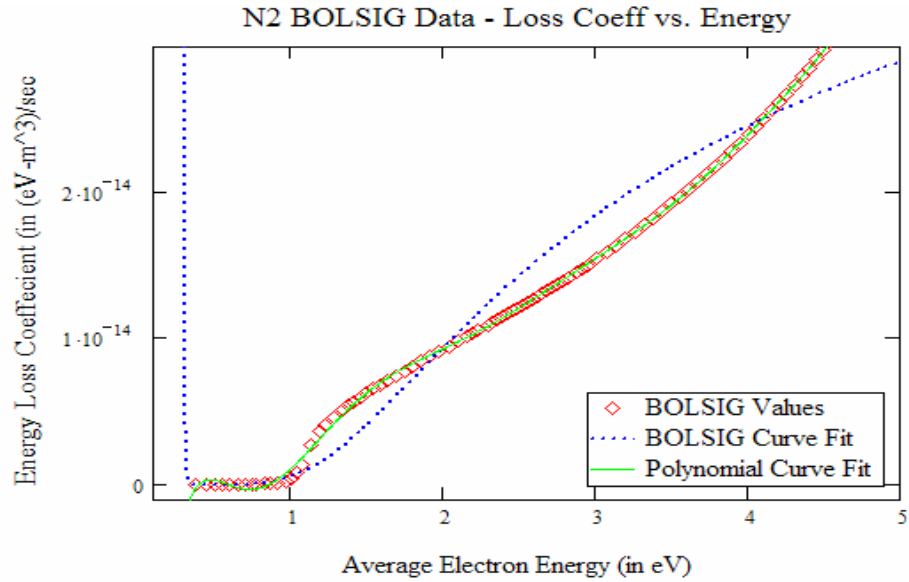


Figure 7. Computational fit for the k_L coefficient as a function of average energy.

In the first graph, the fit obtained from BOLSIG was determined to be accurate enough to use for this project, the second was fitted to a more appropriate polynomial to

more accurately simulate the discrete BOLSIG results. These fits were calculated for the range 0.0-5.0 eV and were determined to be in good agreement with the calculated values in the range 0.3-4.75 eV, therefore upper and lower boundaries were placed on the average electron energy, as to not incorrectly describe the rate and transport coefficients by using the fits to calculate them in a region where they are not appropriately represented. An example of this limiting factor can be seen in the behavior of the fit for the energy loss coefficient above where the value of the polynomial fit drops below zero at around 0.3 eV.

The last set of unknowns, potential and electric field values, for all points on the computational grid must now be determined in order to arrive at a solution of the continuity and electron energy equations. Since the computational set-up will include regions of different permittivity, Gauss's law in the presence of dielectrics must be used to accurately account for any bound charge which might contribute to the polarization of the material under an applied electric field (10:175-180). This law in equations form is:

$$\vec{\nabla} \cdot \vec{D} = \rho_f. \quad (35)$$

\vec{D} is the electric displacement vector defined by $\vec{D} \equiv \epsilon_0 \vec{E} + \vec{P}$, where ϵ_0 is the permittivity of free space, \vec{E} is the electric field in the material, and \vec{P} is the dipole moment per unit volume. The vector \vec{P} is used to correctly account for the bound charge density associated with polarization by an externally applied electric field in a dielectric material. In linear media \vec{P} , can be further defined as $\vec{P} \equiv \epsilon_0 \chi_e \vec{E}$, allowing for a new

equivalent definition of the displacement vector: $\vec{D} \equiv \epsilon_0(1 + \chi_e)\vec{E}$. Finally, making the substitution $\epsilon = \epsilon_0(1 + \chi_e)$ Gauss's law can be rewritten as:

$$\vec{\nabla} \cdot \epsilon \vec{E} = \rho_f \quad (36)$$

where ϵ is the permittivity of the material. Defining this permittivity as a multiple of a *relative* permittivity and the permittivity of free space gives:

$$\epsilon = \epsilon_r \epsilon_0. \quad (37)$$

This *relative* permittivity, ϵ_r , also referred to as the relative dielectric constant of the material, is well known for many materials through experimental measurement. One of the most common dielectric materials used in the aerospace industry today is that of Kapton® tape manufactured by Dupont, with a relative dielectric constant of 4.0; and will therefore be the relative dielectric constant chosen to define the permittivity of the dielectric region(s) between the anode and cathode in this project.

Using the *three-point* formula to solve for the divergence of the electric field in Eq. (36) above, and recalling that the dielectric material being used exhibits linear properties, Gauss's law can be rewritten in 2D as:

$$\frac{\epsilon_{x+\frac{1}{2},y} \vec{E}_{x+\frac{1}{2},y} - \epsilon_{x-\frac{1}{2},y} \vec{E}_{x-\frac{1}{2},y}}{\Delta x} + \frac{\epsilon_{x,y+\frac{1}{2}} \vec{E}_{x,y+\frac{1}{2}} - \epsilon_{x,y-\frac{1}{2}} \vec{E}_{x,y-\frac{1}{2}}}{\Delta y} = \rho'_{x,y}. \quad (38)$$

The free charge on the right hand side of the equation is: $\rho_{x,y}^t = q(n_{x,y}^{i,t-1} - n_{x,y}^{e,t-1})$. The electric field component in Eq (38) above can be defined in terms of the negative gradient of the potential as:

$$\vec{E} \equiv -\vec{\nabla} \phi. \quad (39)$$

Therefore, substitutions can be made for the individual components in Gauss's law as:

$$\begin{aligned} \vec{E}_{x+\frac{1}{2},y} &= -\left(\frac{\phi_{x+1,y} - \phi_{x,y}}{\Delta x} \right) \\ \vec{E}_{x-\frac{1}{2},y} &= -\left(\frac{\phi_{x,y} - \phi_{x-1,y}}{\Delta x} \right) \\ \vec{E}_{x,y+\frac{1}{2}} &= -\left(\frac{\phi_{x,y+1} - \phi_{x,y}}{\Delta y} \right) \\ \vec{E}_{x,y-\frac{1}{2}} &= -\left(\frac{\phi_{x,y} - \phi_{x,y-1}}{\Delta y} \right) \end{aligned} \quad (40)$$

Furthermore, using the previously defined assumption for this project that $\Delta x = \Delta y$, the equation reduces to:

$$-\varepsilon_{x,y-\frac{1}{2}} \phi_{x,y-1} + (\varepsilon_{x+\frac{1}{2},y} + \varepsilon_{x-\frac{1}{2},y} + \varepsilon_{x,y+\frac{1}{2}} + \varepsilon_{x,y-\frac{1}{2}}) \phi_{x,y} - \varepsilon_{x,y+\frac{1}{2}} \phi_{x,y+1} = \rho_{x,y} (\Delta x)^2 + \varepsilon_{x+\frac{1}{2},y} \phi_{x+1,y} + \varepsilon_{x-\frac{1}{2},y} \phi_{x-1,y}. \quad (41)$$

Combining like terms, and assuming that the values of ε are equal over the region of interest, leaves the final form of Gauss's law as:

$$-\phi_{x,y-1} + 4\phi_{x,y} - \phi_{x,y+1} = \frac{\rho_{x,y} (\Delta x)^2}{\varepsilon} + \phi_{x+1,y} + \phi_{x-1,y}. \quad (42)$$

However, if the values of ε vary over the spatially discrete grid, meaning a dielectric interface is encountered, Gauss's law take on the form:

$$-\varepsilon_{x,y-\frac{1}{2}}\phi_{x,y-1} + 2(\varepsilon_{x,y+\frac{1}{2}} + \varepsilon_{x,y-\frac{1}{2}})\phi_{x,y} - \varepsilon_{x,y+\frac{1}{2}}\phi_{x,y+1} = \sigma_{x,y}\Delta x + \left(\frac{\varepsilon_{x+\frac{1}{2},y+\frac{1}{2}} + \varepsilon_{x+\frac{1}{2},y-\frac{1}{2}}}{2}\right)\phi_{x+1,y} + \left(\frac{\varepsilon_{x-\frac{1}{2},y+\frac{1}{2}} + \varepsilon_{x-\frac{1}{2},y-\frac{1}{2}}}{2}\right)\phi_{x-1,y}. \quad (43)$$

This is because the value of ρ_f at any of these points for this project is defined as zero, the value of ε at the dielectric interface has been defined as:

$$\varepsilon_{x\pm\frac{1}{2},y} = \frac{\varepsilon_{x\pm\frac{1}{2},y+\frac{1}{2}} + \varepsilon_{x\pm\frac{1}{2},y-\frac{1}{2}}}{2}. \quad (44)$$

Any accumulated free charge on the dielectric surface has been accounted for by substituting $\sigma_{x,y} = \rho_{x,y}\Delta x$ into Gauss's law. Modeling the dielectric in the system as *sticky*, that is any flux of plasma species incident on the surface adheres and remains at the location of incidence and assuming that any neutralization of the charge species by recombination takes place instantly at the surface, σ can be defined as the accumulation over time of any fluxes incident on the surface. The surface charge density will be calculated using:

$$\sigma_x^t = \sigma_x^{t-1} + q\left(\left|\vec{\Gamma}_{x,y+\frac{1}{2}}^{i,t-1}\right| - \left|\vec{\Gamma}_{x,y+\frac{1}{2}}^{e,t-1}\right|\right)\Delta t \quad (45)$$

reflecting the fact that the dielectric surface for the 2D geometry in this project will be constrained to lie exclusively along the X-axis. A more accurate approximation of the surface charge accumulation and relaxation, could be obtained by adding the term:

$$(-\sigma_{\text{conductivity}} \vec{E}_{\text{interface}} \cdot \hat{n}) \Delta t \quad (46)$$

to the previous equation if the charge on the surface was negative, which represents the rate at which electrons will flow through the dielectric, or the dielectric relaxation time. However, if this term was included, a more complicated description of the surface charge, including emission from the dielectric under appropriate field conditions, would have had to be considered. Therefore, the choice was made to simply consider any charge incident on the surface as *sticky* and not allowed to leave, only recombine.

The previously defined equations for the potential at individual grid points can be united to solve an entire line of potential values in space simultaneously by casting them into a matrix of tridiagonal form. An example of this matrix for a 1D computational region divided into $N = 9$ potential points, with potential points 0 and 8 being specified and one dielectric interface at point 4 is shown below.

$$\begin{pmatrix} 2 & -1 & 0 & 0 & 0 & 0 & 0 \\ -1 & 2 & -1 & 0 & 0 & 0 & 0 \\ 0 & -1 & 2 & -1 & 0 & 0 & 0 \\ 0 & 0 & -\epsilon_{x,y-\frac{1}{2}} & \epsilon_{x,y-\frac{1}{2}} + \epsilon_{x,y+\frac{1}{2}} & -\epsilon_{x,y+\frac{1}{2}} & 0 & 0 \\ 0 & 0 & 0 & -1 & 2 & -1 & 0 \\ 0 & 0 & 0 & 0 & -1 & 2 & -1 \\ 0 & 0 & 0 & 0 & 0 & -1 & 2 \end{pmatrix} \begin{pmatrix} \phi_{x,1} \\ \phi_{x,2} \\ \phi_{x,3} \\ \phi_{x,4} \\ \phi_{x,5} \\ \phi_{x,6} \\ \phi_{x,7} \end{pmatrix} = \begin{pmatrix} \phi_{x,0} \\ 0 \\ 0 \\ \sigma_{x,4} \Delta x \\ \rho_{x,5} (\Delta x)^2 \\ \rho_{x,6} (\Delta x)^2 \\ \rho_{x,7} (\Delta x)^2 + \phi_{x,8} \end{pmatrix} \quad (47)$$

The equation above corresponds to the 1D set-up shown below in Fig 8. Squares denote locations at which the potential is calculated as well as the value of any free charge in the

system. Surface charge is allowed to accumulate on the dielectric surface for this example. X's indicate where the fluxes between points will be calculated.

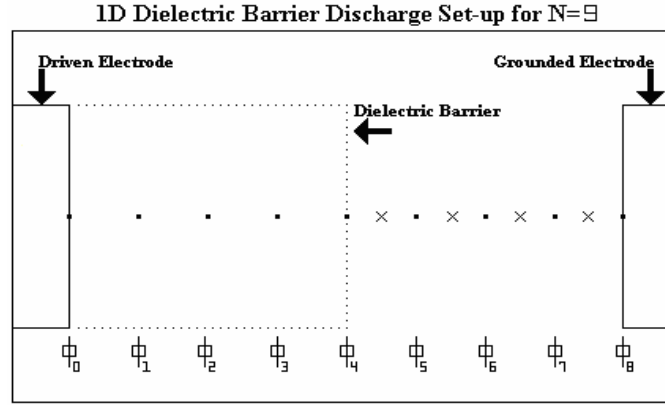


Figure 8. Set-up for the DBD device as described by Eq (47).

Notice that no free charge is allowed to exist in the dielectric, and that the actual numbering of the points goes from 0 to 8, for a total of 9 points, to be consistent with the formalism of starting array elements in matrices at zero. This matrix can be easily solved for by using the Thomas algorithm (5:285). The Thomas algorithm is a direct, single pass method of solving a tridiagonal matrix. The 1D approximation used here is justified when the length and width of the electrodes is much greater than the spacing between them, the exact value of the potential can then be directly obtained using the Thomas algorithm. This is because the potential at all points perpendicular to the point of interest are equivalent in value in this 1D problem, which is why the matrix shown in Eq (47) is tridiagonal. However, in the 2D formalism, an iterative scheme is used to converge upon an approximately correct solution for the scalar potential points over the computational domain. This is because the electrodes and free charges are no longer considered to be

infinite sheets or over a domain that is much, much bigger than the spacing of the electrodes.

The iterative method invoked for the 2D representation is basically a 5-point averaging method. The four closest points around the point of interest are averaged to find a new value for the fifth point. The notable difference between the approach used in this project and the standard 5-point method is that all the points along a given axis are implicitly solved for, using the notional set-up shown below. This line method should theoretically take a little longer for each iteration of the system than the 5-point averaging method, but convergence to the set tolerance should happen in half the number of iterations (5:285).

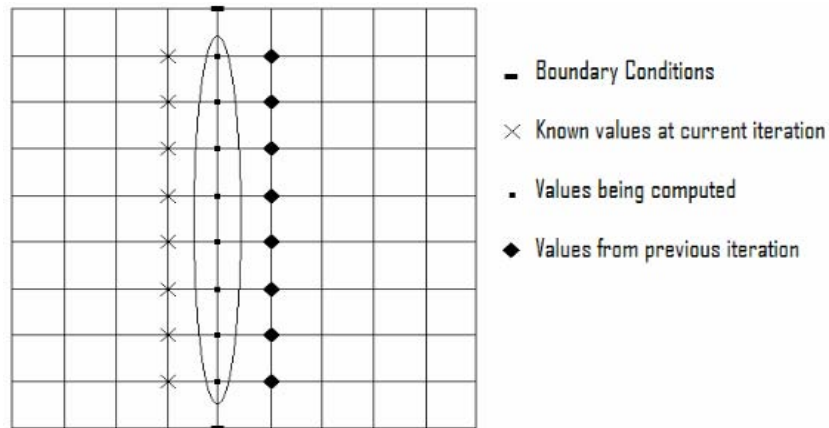


Figure 9. Line method used for solving the 2D potential profile.

The convergence criterion of the 2D potential solver requires that all potential points in the computational domain vary by less than 10^{-6} in value, between their previous iteration value and the current value. This criterion resulted in a substantial number of iterations during the first time step but resulted in significant computational

time savings for subsequent time step intervals. This is because the line method described above saves and uses the previous potential values from the prior time, and uses them as a starting value for each subsequent time step. If the time step of the system is small enough, and the charged particles have not moved very much, then only a few iterations are required to find the new potential values. For large systems, the line method described above should give substantial computational time savings over the 5-point method, but a detailed comparison was not made.

Values for the electric field can then be determined by taking the negative of the gradient of the potential for every location between points in the computational area.

III. Computational Set-up and Potential Solver

1D Computational Set-up

The 1D computational set-up is shown below.

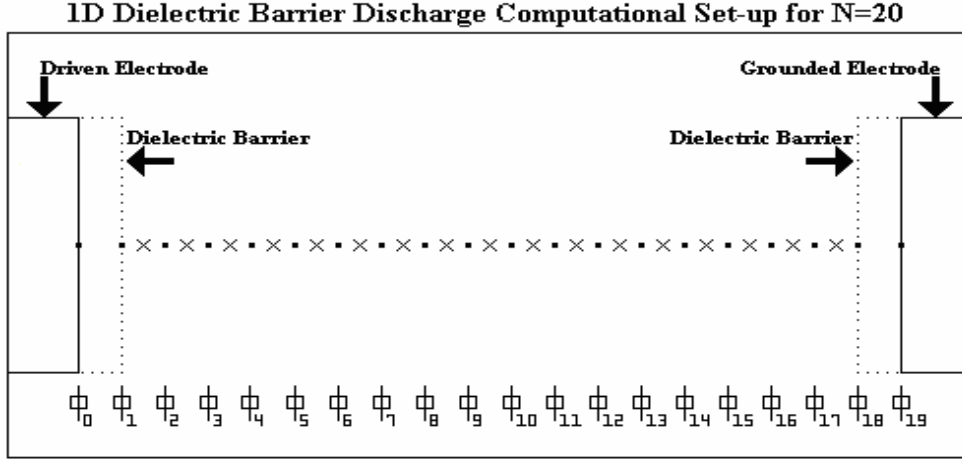


Figure 10. Characteristic set-up geometry for the 1D numeric model.

A staggered grid is employed where points labeled by squares are where the potential, number density, average electron energy are solved for and tracked, as well as values for the associated permittivities, mobilities, and diffusion coefficients. These locations are indicated with a whole number value. X's indicate where electric field values, particle and energy fluxes, and other half-point values identified as necessary for the solution to the three governing equations are evaluated. Notice that the dielectric boundary could extend over many computation points, or simply be removed altogether to simulate an exposed electrode.

The first step in determining whether or not the numeric code used in this project was correct was to validate the potential solver by comparing the results to an analytically

derived solution or to other computational results. Results are shown below for a 1D system with no dielectric barriers and no space or surface charge present.

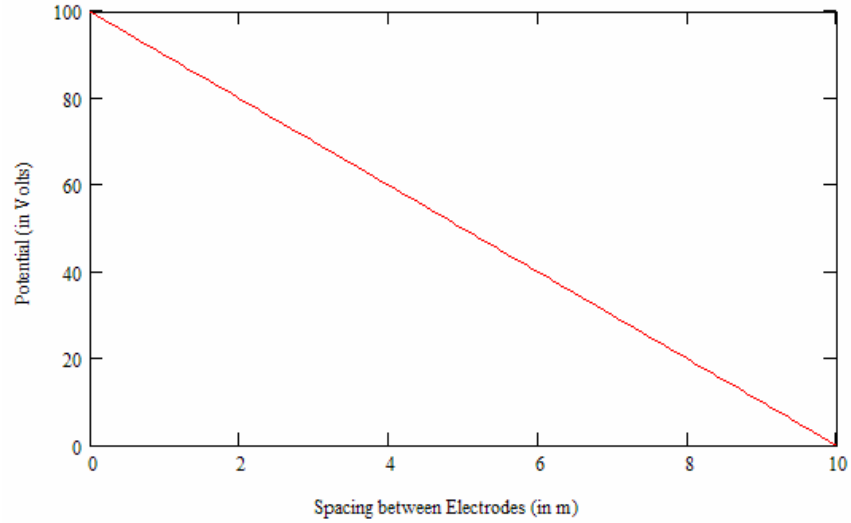


Figure 11. Potential profile for 1D region with no dielectrics or free charge.

Here a potential of 100 volts was applied to the left electrode, while the right electrode was grounded. The potential solver correctly returns a linear variation in the absence of any charge between the electrodes. Next, a dielectric region was added to determine the accuracy of the code, with various dielectric materials present between the electrodes. Shown are the results for a region, with a dielectric constant of 4.0, extending from the left electrode to midway between the electrodes. It is easily observed that the value of the electric field (negative gradient of the potential profile) outside the dielectric material is 4.0 times the value inside. This reduction in electric field strength comes from the polarization inside the dielectric, caused by the alignment of bound charge dipoles, counteracting the applied field from the electrodes. This confirms that the conditions for the potential solver with dielectric material present are correct.

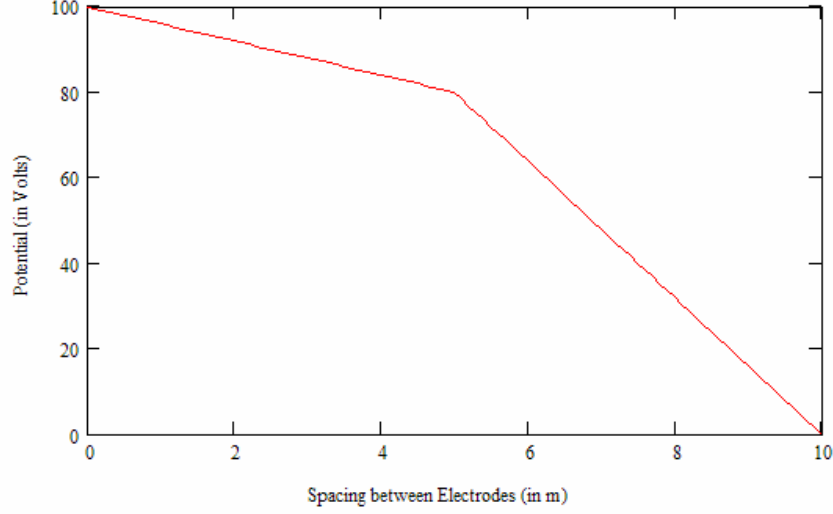


Figure 12. Potential profile for inserted dielectric and no free charge.

With the addition of space and surface charge to the system, the computational code for the solver becomes a bit more complicated, making validation under these circumstances especially important. The analytic result for the addition of a uniform space charge to a 1D system, with an electrode spacing of L is:

$$\phi(x) = \frac{-\rho_{space}}{2\epsilon_0} x^2 + \left(\frac{\phi_{right} - \phi_{left}}{L} + \frac{\rho_{space}}{2\epsilon_0} L \right) x + \phi_{left} \quad . \quad (48)$$

The boundary conditions at the electrodes are again set to 100 volts and ground, for the left and right side respectively. In this case, the uniformly distributed positive charge introduced is 10^{-10} C/m^3 , and the number of evaluation points for the solver is $N=100$. Computational results, shown as X 's, are superimposed on the analytic solution, shown as a line, in the figure below. Greater accuracy could have been obtained at the cost of computational time by adding more points to the simulation; but every

calculated point was within 10^{-6} volts of the analytic answer, and this was deemed adequate for the project purposes.

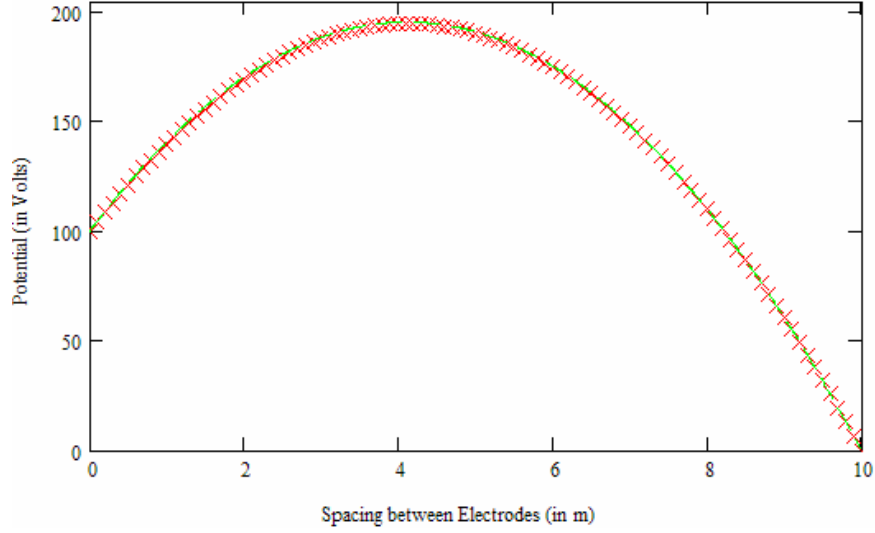


Figure 13. Potential profile for no dielectrics and positive free charge.

Finally, with the 1D potential solver tested for various dielectric materials and space charge, conditions needed to be implemented for handling multiple dielectric regions within the computational area and to account for any accumulated surface charge on the dielectric surfaces. The results from these additions are shown below. Dielectric material with a permittivity of $4\epsilon_0$ has been introduced covering both electrodes. Each had a thickness of 2 mm, the boundaries of which can be seen at the X-axis positions of 2 mm and 8 mm in the figure below. Surface charge in the amount of $-2.0 \cdot 10^{-6} \text{ C/m}^2$ and $2.0 \cdot 10^{-6} \text{ C/m}^2$ has been introduced to the left and right dielectric surfaces respectively, as well as a uniformly distributed positive charge between the electrodes of $1.5 \cdot 10^{-4} \text{ C/m}^3$. It should be noted, that Fig 14 below indicates that with enough surface charge accumulated on the dielectric surfaces, the electric field inside the active region of

a DBD device could be significantly reduced, leading to discharge extinction under DC operating conditions.

By defining:

$$\begin{aligned}
\alpha_1 &\equiv \frac{\varepsilon_0}{D_2 - D_1} + \frac{\varepsilon_1}{D_1} \\
\alpha_2 &\equiv \sigma_1 + \frac{\rho}{2}(D_2 - D_1) + \frac{\varepsilon_1}{D_1}\phi_{Left} \\
\alpha_3 &\equiv \left(\frac{D_2 - D_1}{\varepsilon_0} \right) \left(\frac{\varepsilon_2}{D_2 - L}\phi_{Right} - \sigma_2 - \rho D_2 + \frac{\rho}{2}(D_2 + D_1) \right) \\
\alpha_4 &\equiv 1 - \frac{\varepsilon_2}{\varepsilon_0} \left(\frac{D_2 - D_1}{D_2 - L} \right) \\
\phi_{D1} &\equiv \frac{\alpha_1 \alpha_2 \alpha_4 (D_2 - D_1)}{\alpha_1^2 \alpha_4 (D_2 - D_1) - \alpha_1 \varepsilon_0} - \frac{\varepsilon_0 \alpha_3}{\alpha_1 \alpha_2 (D_2 - D_1) - \varepsilon_0} \\
\phi_{D2} &\equiv \frac{\phi_{D1} - \alpha_3}{\alpha_4}
\end{aligned}$$

where the ϕ 's represent potential values at specified points, σ 's represent the surface charge, ρ represents the space charge, the ε 's represent the dielectric constant of the material and the D 's and L represent the location of the dielectric surfaces and the spacing of the electrodes respectively, the parametric analytic solution of the potential in the three regions shown from left to right in Fig 14, can be written:

$$\begin{aligned}
\Psi_I(x) &= \frac{\phi_{D1} - \phi_{Left}}{D_1} x + \phi_{Left} \\
\Psi_{II}(x) &= -\frac{\rho}{2\varepsilon_0} x^2 + \left(\frac{\phi_{D2} - \phi_{D1}}{D_2 - D_1} + \frac{\rho}{2\varepsilon_0}(D_2 + D_1) \right) (x - D_1) + \frac{\rho}{2\varepsilon_0} D_1^2 + \phi_{D1} \cdot \quad (49) \\
\Psi_{III}(x) &= \left(\frac{\phi_{D2} - \phi_{Right}}{D_2 - L} \right) (x - L) + \phi_{Right}
\end{aligned}$$

The location of the pertinent variables have been labeled in the figure below. N in the calculation of the numeric solution has again been set to 100. X's are the numeric solution calculation points which overlay the analytic solution represented by a line. The two results are in excellent agreement, and show that the potential solver in 1D is indeed accurate.

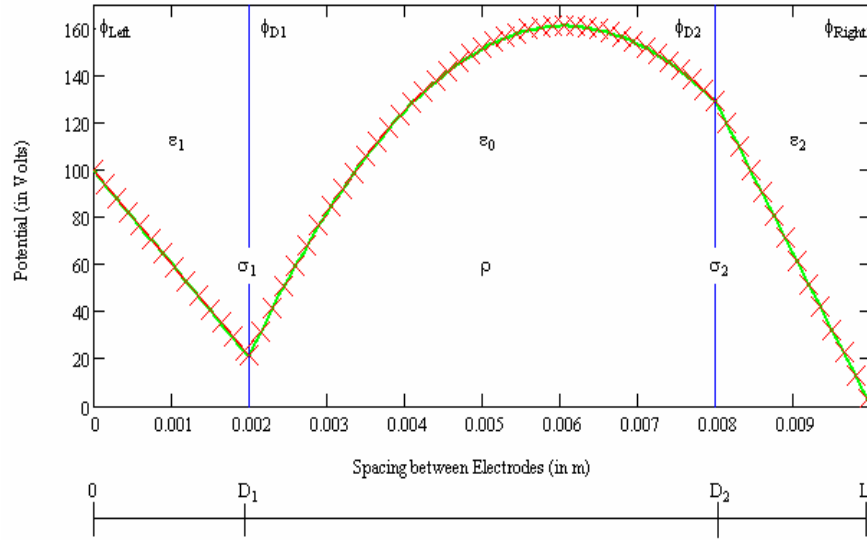


Figure 14. Potential profile for inserted dielectrics with free charge.

With the results of the potential solver deemed satisfactory, the resultant potential values, and thus electric field values can be sequentially introduced to the continuity and electron energy equations described in Chapter 2, completing the last of the unknowns in the governing equations. Shown below is the highest level algorithm for describing the iterative process by which these equations will be solved for in this project. Starting with appropriate initial conditions, the governing equations can be solved in this iterative manner to approximate the temporal evolution of the system. More results of the 1D code will be discussed in Chapter 4. Serious consideration was given to using a

completely implicit method, and solving for all the equations simultaneously at any given time step. However, the time step size required for stability reported by Marchand (15:84) for the fully implicit method was less than that of the sequential method. Therefore, the sequential method was chosen for both the 1D and 2D geometries. This greatly simplified the numerical complexity, while still allowing for an accurate solution in a reasonable amount of time.

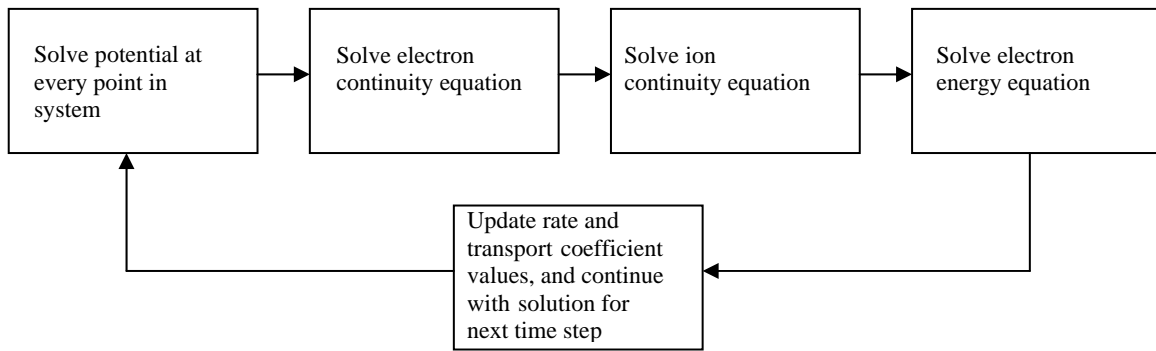


Figure 15. Semi-implicit algorithm for solving the governing equations.

2D Computational Set-up

The 2D computational set-up is shown below.

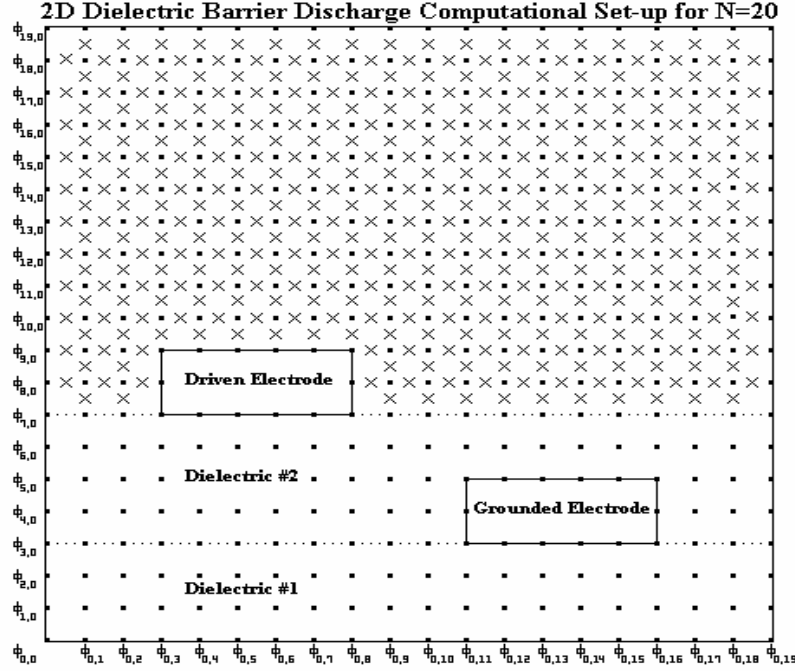


Figure 16. Characteristic set-up geometry for the 2D numeric model.

Like the 1D set-up, squares represent whole number values on the grid, indicating where potential, number density and electron energy density values are tracked and recorded. X's are at the half-point values, associated with the fluxes and the electric field values between whole point locations. Migrating the code from a 1D to 2D set-up was simplified by assuming a superposition principle for the system, where the 2D set-up could be described using its 1D components. This superposition principle was particularly advantageous, given the 1D characteristic of the fluxes in the governing equations, as defined in Chapter 2. Values for the number and energy densities at each point were found by solving the tridiagonal governing equations along a particular axis.

The changes in the value of the points due to the flux from their neighboring points from the previous time step to the current time step were then recorded. This process was repeated for the other axis, using the initial values from the previous time step. The changes due to the X-axis and Y-axis fluxes were then added to the previous value to find the new value. This approach is notionally shown below.

$$n_{x,y}^{s,t} = n_{x,y}^{s,t-1} + \Delta n_{\text{Due to flux on X-axis}}^s + \Delta n_{\text{Due to flux on Y-axis}}^s$$

This piecewise solving of the new values is incidentally the reason for the inclusion of the $\frac{1}{2}$ in the source and loss terms of the governing equations as discussed earlier. This is because source and loss terms are generally based on the local number density at the previous time step without regard to direction, and are counted twice in the superposition scheme implemented.

Careful consideration was put into correctly describing the boundary conditions for the 2D environment, since the goal of the project was to model a manufacturable, aeronautically realistic configuration. The potential values at the base of the computational area were specified to be at relative ground, since they would in practice be in contact with a conducting aircraft surface. Two different regions of variable dielectric constant were introduced to allow for more flexibility when modeling different construction materials as well as investigating the affects of changing the insulating materials between the aircraft surface and the electrodes. The goal was to correctly describe a simple geometry, which was most like what an experimental configuration might look like. This project does not implement code to examine features of the DBD

device if the grounded electrode is moved underneath the driven electrode, or to account for multiple electrodes as in some experimental set-ups (18:4).

Charge buildup was allowed to accumulate on the top of dielectric #2, the affects of which can significantly influence the potential profile just as it did in the 1D case, as seen below. Fig 17 shows the potential profile, as well as the resulting electric field vectors, for a case in which no surface charge is present. Fig 18 shows the resultant potential and field profile for a case in which a negative surface charge is uniformly distributed on the dielectric surface directly above the grounded electrode. The quantity of the free charge on the surface of the dielectric in the second figure was not recorded, and the MathCAD file used to obtain the results was found to be corrupted. Therefore, the exact surface charge value associated with Fig 18 is not known. Efforts to rebuild the code were done, but with no success. Completely rewriting the code was deemed too time consuming. The presented results do however serve as an example of the change in electric field configuration under charge accumulation conditions. The driven electrode is held at a potential of 100 volts. Notice the abrupt change in the potential profile at the dielectric interface of the Kapton® and air. This is because of the factor of 4.0 change in the permittivity of the two mediums. The electric field vectors near the region of introduced surface charge are also significantly different between the two figures, suggesting that the accumulated free charge on the surface of the dielectric can play an important role in the dynamics of the system, and therefore the flow control associated with various operating parameters.

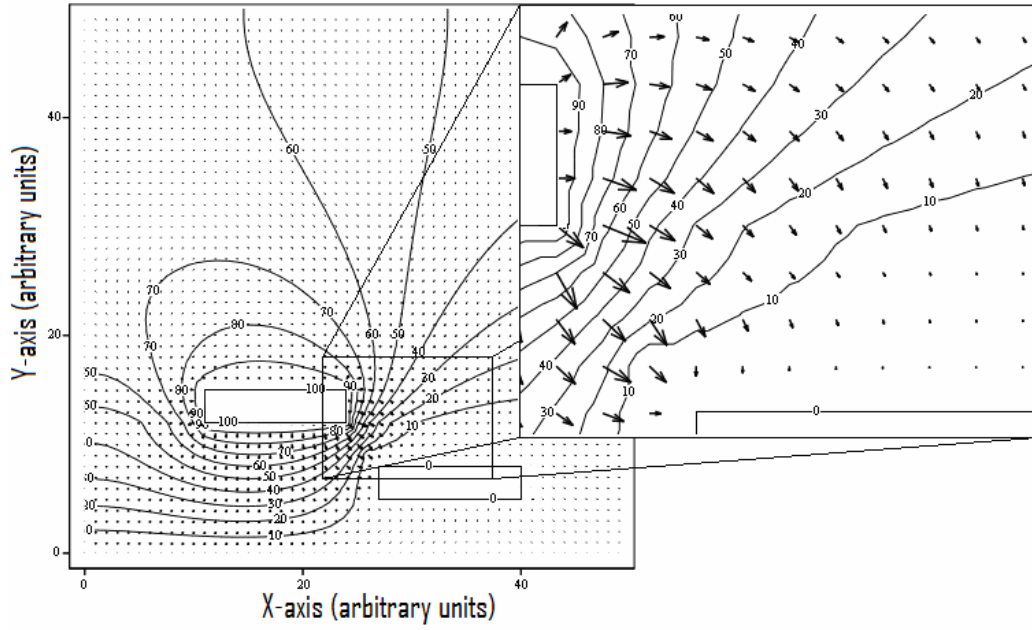


Figure 17. 2D potential profile and associated E field vectors for no free charge.

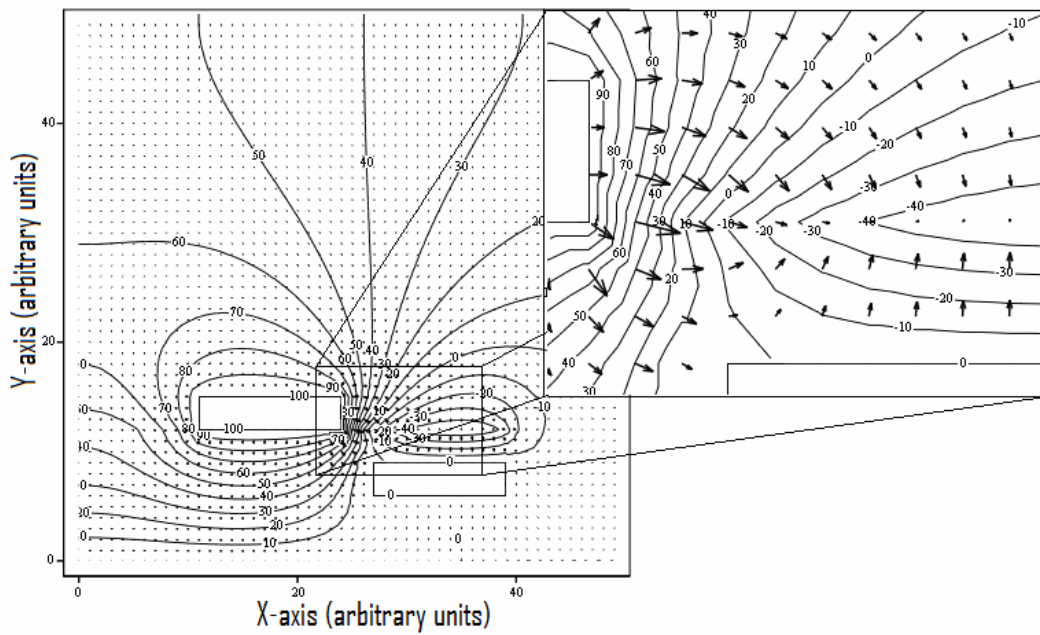


Figure 18. 2D potential profile and associated E field vectors for negative surface charge.

One more potential solver verification was made for the 2D code before integrating it with the governing equations to solve the dynamics of the system. The value of the normal component of the displacement (\vec{D}_\perp) at the interface of the dielectric and gas of the system should be continuous and approach the analytic solution of:

$$\vec{D}_{\perp dielectric} = \vec{D}_{\perp freespace} . \quad (50)$$

It should be noted that the individual X-axis and Y-axis component values of the displacement can be known for the aforementioned 2D geometry because of the systems boundary conditions, and the iterative method used to determine the potential values. This allows for the component contribution to the divergence of the displacement by any free charge to be found. If the specified boundaries and spatial discretization of the system are adequate, then one would expect that the perpendicular component of the displacement vector of the solved system approach or come close to the real value.

For this case, no surface charge will be allowed. Rewriting the Eq (50) above into its equivalent dielectric constant and potential components representation along the Y-axis gives:

$$\epsilon_{dielectric} \frac{(\phi_{x,y} - \phi_{x,y-1})}{\Delta x} = \epsilon_{freespace} \frac{(\phi_{x,y+1} - \phi_{x,y})}{\Delta x} , \quad (51)$$

since the values of the displacement vector are solved for at locations of $\pm \frac{1}{2} \Delta x$ above and below the interface point. By further manipulating the equation above, it follows that:

$$\frac{\epsilon_{dielectric}}{\epsilon_{freespace}} = \frac{\frac{(\phi_{x,y+1} - \phi_{x,y})}{\Delta x}}{\frac{(\phi_{x,y} - \phi_{x,y-1})}{\Delta x}}. \quad (52)$$

If a nominal values of $\epsilon_{freespace} \approx 1.0$ and $\epsilon_{dielectric} \approx 4.0$ are specified for the potential solver, it follows that both sides of the equation above should evaluate to 4.0 in the limit that the grid points become arbitrarily close to the dielectric interface. The convergence to the value 4.0, for a point on the interface, lying halfway between the start and end of the grounded electrode for increasing values of N , corresponding to smaller and smaller spacing between the potential points, is shown in the table below. The length and width of the computational region is 0.1 meter, defining $\Delta x \equiv 0.1/N$, and the convergence tolerance was set to 10^{-8} . Values of the time to convergence for the solver were also recorded, as well as their associated computational iteration cost. Notice that for increasing value of N (or more closely spaced calculated potential points, given better spatial resolution to the system) the time to convergence is approximately quadrupled for every doubling of the resolution. The potential solution is in fact the most computationally intensive portion of the total solution, so the number of calculation points was held at $N = 50$ for the remainder of the project, to allow for results to be obtained within a reasonable amount of time.

Table 1. Computational values for the electric field converging on the analytic solution.

Value of N	$\vec{E}_{\perp Above} / \vec{E}_{\perp Below}$	Iterations to Convergence	Time to Convergence
50	3.312	$\approx 8,000$	< 30 sec
100	3.742	$\approx 32,000$	≈ 1 min
150	3.840	$\approx 74,000$	≈ 3 min
200	3.862	$\approx 124,000$	≈ 10 min
250	3.883	$\approx 190,000$	≈ 45 min

The 2D potential solver was further validated by coding its geometry to simulate the 1D environment. This was done by modifying the boundary conditions to make the top and bottom of the computational region electrodes. The side boundary conditions remained set to ensure no perpendicular field components, thus reproducing the 1D approximations. The results from the modified 2D code, matched the 1D code perfectly for a series of test, including single dielectric, multiple dielectrics, and space and surface charge presence, and the analytically derived uniform space charge presence. A representative result of this pseudo 1D code is shown in Fig 19 below. No free charge was present in the system and a dielectric of relative constant 4.0 was inserted from the left electrode to midway between the electrodes. Comparing this 2D result with the 1D result shown in Fig 11, shows that they are identical. The last validation for the 2D code was done by using the standard 5-point averaging method in Microsoft Excel under identical point geometry to solve for the potential profile without space charge present, and comparing the outputs of both programs. As seen below in Fig 20 for a small portion of the results near the electrodes, the comparison matched up perfectly, and helped established further confidence in the 2D potential solver.

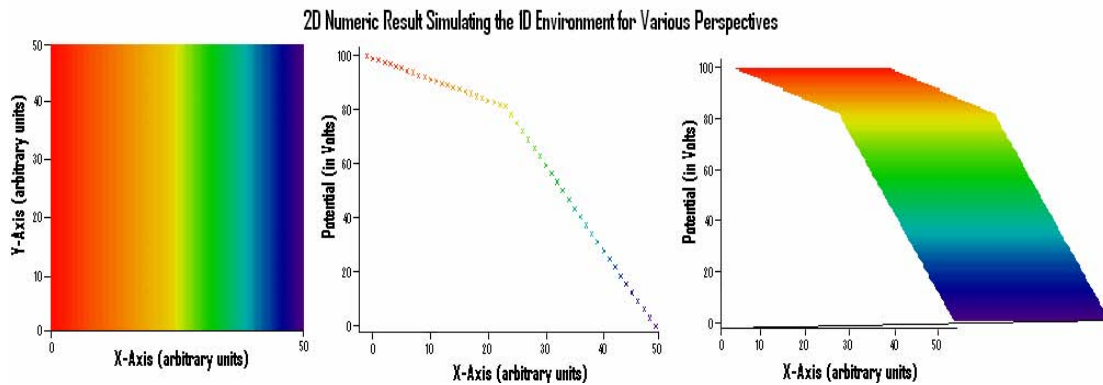


Figure 19. The 2D potential solver results for a pseudo 1D geometry.

Excel Results			Numeric Code Results		
41.5892644	38.64189843	35.35925385	4.158926e+001	3.864190e+001	3.535925e+001
44.543817119754	40.273882505125	35.883112142282	4.454382e+001	4.027388e+001	3.588311e+001
50	42.026702330137	36.004220219998	5.000000e+001	4.202670e+001	3.600422e+001
50	41.828706595423	34.975244717763	5.000000e+001	4.182871e+001	3.497524e+001
50	40.312879333792	32.583516441306	5.000000e+001	4.031288e+001	3.258352e+001
50	36.839294298439	28.358373717306	5.000000e+001	3.683929e+001	2.835837e+001
36.346187571105	28.685924142656	21.556090243976	3.634619e+001	2.868592e+001	2.155609e+001
26.797795318846	20.002124457105	12.645952478869	2.679780e+001	2.000212e+001	1.264595e+001
19.422864582977	11.878825888048	0	1.942286e+001	1.187883e+001	0.000000e+000
14.474144191556	8.090314512111	0	1.447414e+001	8.090315e+000	0.000000e+000
11.129810128911	6.008287968841	0	1.112981e+001	6.008288e+000	0.000000e+000
8.804726706153	4.813027234343	0	8.804727e+000	4.813027e+000	0.000000e+000
7.149608047216	4.439094262376	1.912694719697	7.149608e+000	4.439094e+000	1.912695e+000
5.711456839952	3.881047048250	2.283872976059	5.711457e+000	3.881047e+000	2.283873e+000

Figure 20. 5-point averaging Excel and numeric code results for similar regions.

IV. Results and Conclusions

The results for various cases using the 1D code are shown and discussed below. Electrode potentials are modeled as DC for all the results, even though DBD actuators are run in an AC mode. The DC approximation is sufficient for the time scales investigated. The time step used for all the simulations was 10^{-10} seconds. This is about two orders of magnitude smaller than what the dielectric relaxation time t_{di} , defined by:

$$t_{di} = \frac{\epsilon_0}{q(n^e \mu^e + n^i \mu^i)} \quad (53)$$

was expected to be, but still not so small as to require an inordinate amount of computational time per simulation.

The code was migrated to the 2D environment; but unfortunately inherent problems with the boundary conditions in the governing equations, instabilities and errors in the code, discovered late in the project, kept the ultimate goal of modeling a realistic interaction between the charged species and the neutral particles from being accomplished.

DC Discharge Sheath Test

The first characteristic test chosen to see if the electron and ion continuity equations returned accurate, expected results when integrated with the potential solver and solved sequentially, was to look at the DC discharge sheath that forms during the first few nanoseconds of the discharge. Under DC operating conditions, it should be expected

that the electrons, because of their relatively high mobility, as compared to the ions would move under any applied field in the system quickly, leaving the resulting plasma with a *sheath* formation. This *sheath* of positively charged plasma should remain close to the cathode as electrons are forced toward the anode. This depletion causes a secondary electric field, that acts to shield the rest of the plasma from the anode, and it remains in its quasi-neutral state. A sheath region should also develop around the anode, as electrons are lost to the surface of the electrode or dielectric coating due to the applied electric field and their high thermal velocities. Results for the 1D system with (Fig's 21, 22, and 23.) and without (Fig's 24, 25, and 26.) dielectrics as thin coatings on the electrode surfaces are shown below. Charge densities for the electrons and ions are plotted normalized to their initial condition, which in these cases was a uniform distribution. Parameters for this test, with Ar gas and the anode held constant at -50 volts, were held constant as follows:

$$\begin{array}{lll}
 n^e = n^i = 10^{15} \text{ /m}^3 & u^e = 1.0 \text{ eV} & P = 100 \text{ Torr} \\
 \mu^e = 0.3 \text{ m}^2 \text{ /V / s} & \mu^i = 10^{-3} \text{ m}^2 \text{ /V / s} & \nu = 0.0 \\
 D^e = 0.3 \text{ m}^2 \text{ / s} & D^i = 10^{-4} \text{ m}^2 \text{ / s} & \beta = 0.0
 \end{array}
 .$$

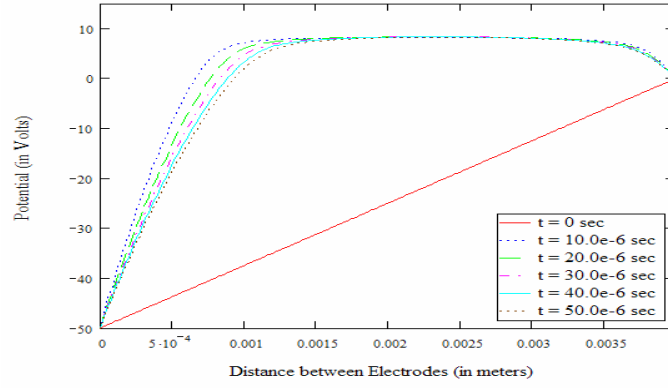


Figure 21. Potential profile during formation of the DC discharge sheath in a system with bare electrodes.

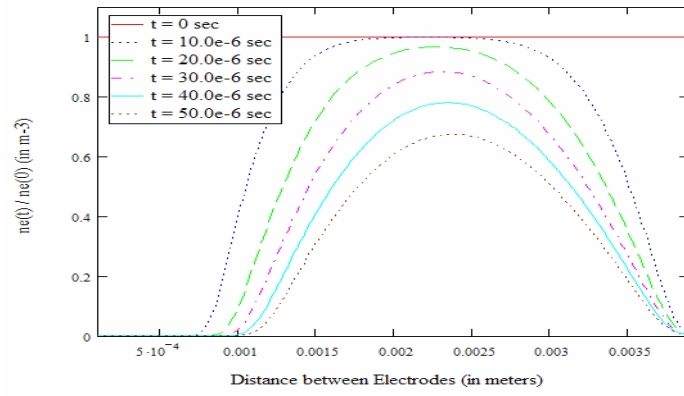


Figure 22. Normalized electron density during formation of the DC discharge sheath in a system with bare electrodes.

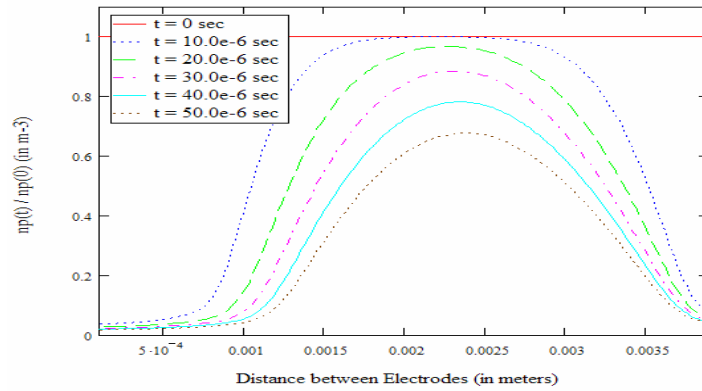


Figure 23. Normalized ion density during formation of the DC discharge sheath in a system with bare electrodes.

The width of the sheath region for the results above is approximately 0.001 m . This is consistent with the method used by Poggie to estimate the region width (16:2). The characteristic width should be on the order of a Debye length defined as follows:

$$\lambda_{Debye} = \left(\frac{\epsilon_0 k_b T_e}{n^e q^2} \right)^{\frac{1}{2}} . \quad (54)$$

Estimating the electron temperature to be approximately 10,000° K or about 1.0 eV, it can be shown that $\lambda_{Debye} = 0.000218 m$, indicating that the sheath region observed in these calculations is about five Debye lengths wide. This is of the order that was expected, and was therefore deemed a reasonable result.

Notice that the charge accumulated on the dielectric surfaces of the figures below affects the potential profile and width of the sheath region. It is also seen that many more charged particles are left in the system with dielectric coatings. This is because of the reduced field caused by the accumulation of charge on the dielectrics, and the fact that the charges are not allowed to leave the system through the electrode as before.

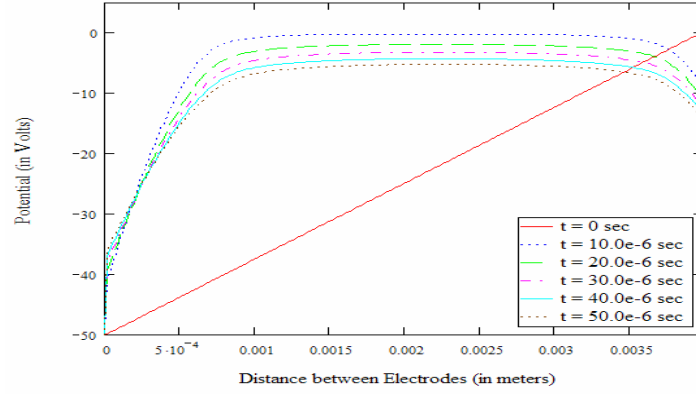


Figure 24. Potential profile during formation of the DC discharge sheath in a system with dielectrics coatings.

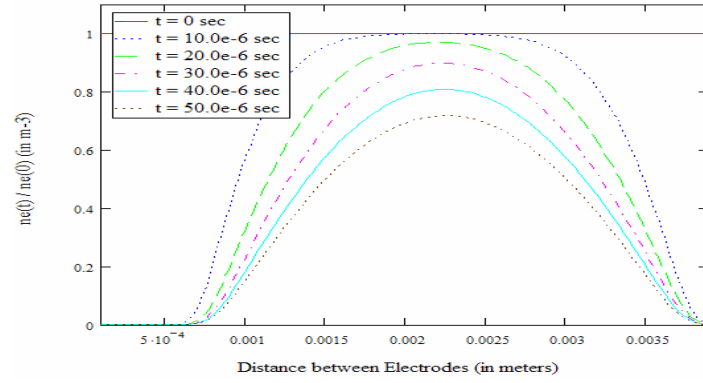


Figure 25. Normalized electron density during formation of the DC discharge sheath in a system with dielectric coatings.

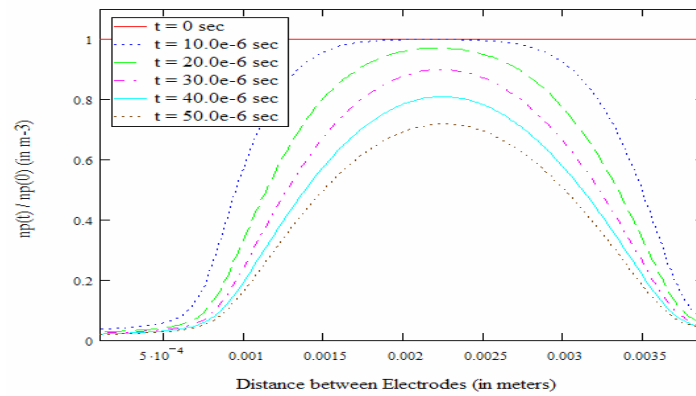


Figure 26. Normalized ion density during formation of the DC discharge sheath in a system with dielectric coatings.

The results showed good agreement of the electron density with previous numeric calculations as seen in Fig 27. In Fig 27 the number density is not normalized to the initial condition. The ion densities differ, and this subsequently affects the calculated potential profile (12:11).

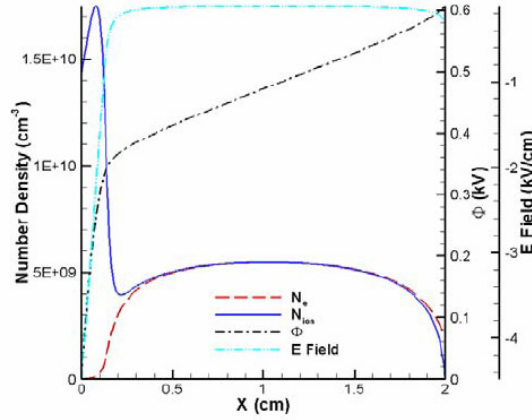


Figure 27. DC discharge results reported by Hilbun (12:11)

Ambipolar Diffusion

For no applied potential across the electrodes and an initially quasi-neutral plasma distribution, the charged particle density near the electrodes should exhibit a rapid depletion of the electrons, due to their much higher thermal speed than that of the ions. As electrons are lost to the boundaries much more quickly than the ions, an induced electric field is formed that tries to bring the system back to its quasi-neutral state by balancing the fluxes. This process of the plasma, where diffusion dominates the first few time steps and then the induced field effect starts to limit the process, is seen in Fig's 28 and 29 for various time steps below. The initial conditions for the system were that both electrodes be held at ground with dielectric coatings present, and that the plasma be distributed sinusoidally as follows:

$$n_x^e = n_x^i = n(0) \sin\left(\frac{\pi x}{L}\right), \quad (55)$$

with $n(0) = 10^{14} / \text{m}^3$. The transport coefficients were determined using the BOLSIG fits with the electron energy held constant at 1.0 eV, in a 1 Torr gas of N_2 . Ionization and recombination were set to 0. The plots below in Fig's 28 and 29 show the relative changes in number density as the system transitions from a diffusion to an ambipolar particle flux.

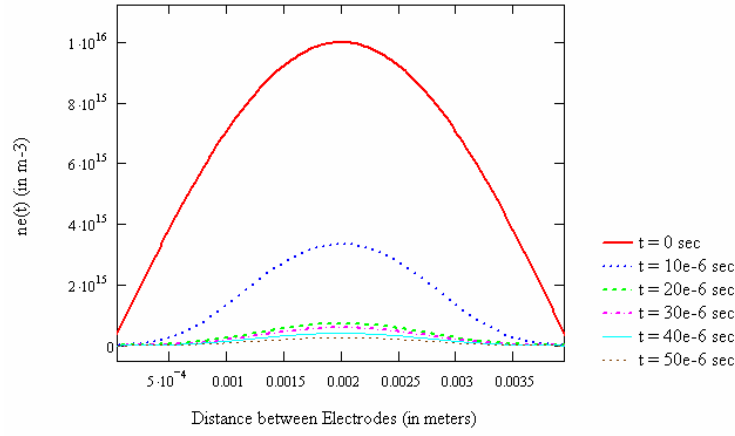


Figure 28. Electron density during ambipolar diffusion.

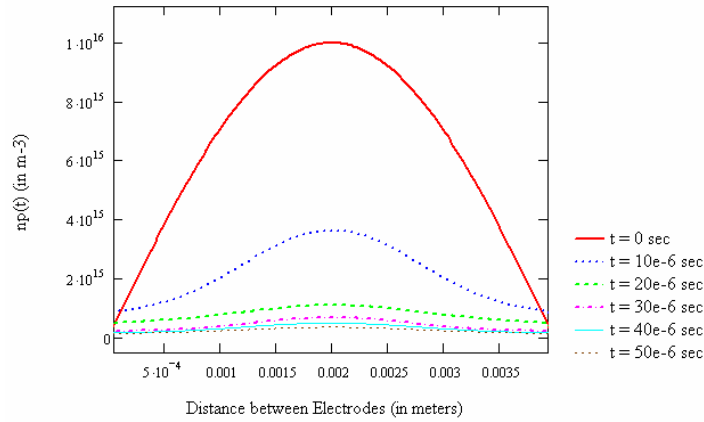


Figure 29. Ion density during ambipolar diffusion.

This non-uniform decay shown above is indicative of the induced electric field which results from the initial charge separation caused by the fast moving electrons. It should also be noted that the system has not yet reached an equilibrium point for the time steps shown. Fig 29 shows an initial build-up of positively charged ions near the dielectric boundaries, and could be indicative of a *bottleneck* in the numeric method due to an unrealistic boundary conditions, or an error in the code. The source of the apparent problem was never clarified. An immediate rise in the potential profile over the entire domain was also noticed as seen below; but then began to settle back to its initial condition, as should be expected as the system tries to return to a quasi-neutral state.

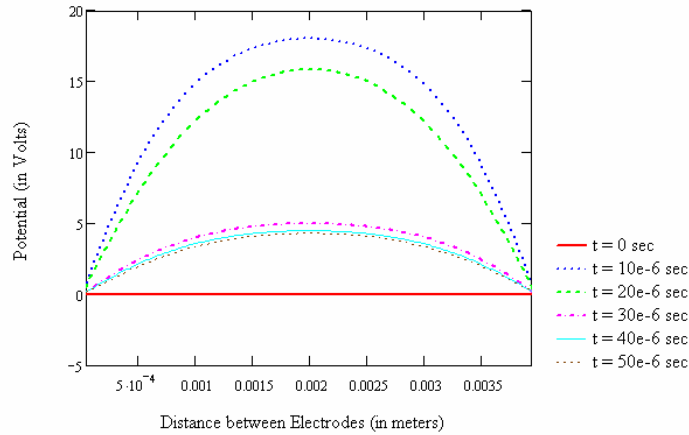


Figure 30. Potential profile during ambipolar diffusion.

Furthermore, the accumulated flux, calculated by the numeric code at the dielectric surfaces (which are in this case one Δx thick, and placed directly over both the anode and the cathode), should average to zero after the system reaches a steady state distribution, as well as be nominally equal to each other as the dynamics of the system develop because of the symmetry involved. Shown in the table below are the results for

the surface charge per meter squared at both dielectric surfaces for various times. Note that the values correctly approach zero as time increases.

Table 2. List of calculated accumulation of surface charge on the dielectric surfaces for various times during ambipolar diffusion.

	Time = 0 sec	Time = 1 μ s	Time = 2 μ s	Time = 3 μ s	Time = 4 μ s	Time = 1ms
Surface Charge on left dielectric	0	-2.0421e-7	-1.5036e-7	-5.3790e-8	-3.9940e-8	-2.2720e-10
Surface Charge on right dielectric	0	-2.0406e-7	-1.5025e-7	-5.3680e-8	-3.9830e-8	-1.2580e-10

Constant Characteristic Parameters Comparison

With the continuity equations tested, a full implementation with the electron energy density equation included, as well as the associated rate and transport fit, was tested. This final test was conducted on the 1D code on a system comprised of 100% N₂ by changing the gas pressure, electrode spacing, and initial charge densities for systems that held the parameters below constant, and observing their behavior over time:

$$\frac{\vec{E}}{N_{Neutral}}, P \times d, \frac{n^{s,0}}{N_{Neutral}}.$$

The first term is called the reduced field, the second is the pressure multiplied by the electrode spacing, commonly associated with the Paschen curve (which describes the breakdown voltage relationship of the system as a function of the pressure of the system and the electrode spacing), and the final term is the fractional ionization of the system.

\vec{E} is the electric field, $n^{s,0}$ is the initial uniform charge density for both species, d is the electrode separation distance, and P the pressure of the neutral gas which is related to

$N_{Neutral}$. This neutral number density was previously defined in Eq (15). The temperature of the system is set to 300° K. The driven electrode, the anode in this test case is located on the left of the 1D environment. The potential of the anode was fixed at 2.5 kV for all cases. This occurs naturally by holding the reduced field term defined above as constant. The governing equations retain the same form for all cases, but values for the neutral number density, the electric field, and the rate and transport coefficients change. The initial rate and transport coefficients remained the same however, because the initial value given to the local electron energy was defined as 3.0 eV at every location in the system. These changes resulted in different behaviors being incorrectly observed for each simulated scenario in this project, in part because of the limitations associated with the rate and transport coefficients as well as the spatial discretization, which changed as the electrode separation changed. In reality, the results should have been identical.

Table 3. Values used for comparison between constant characteristic systems.

Pressure (in Torr)	Electrode Separation (in m)	Charge Density (in m ⁻³)	Potential (in V)
P=1	d=.1	$n^{s,0}=10^{15}$	V=2500
P=10	d=.01	$n^{s,0}=10^{16}$	V=2500
P=100	d=.001	$n^{s,0}=10^{17}$	V=2500
P=350	$d=2.857 \times 10^{-4}$	$n^{s,0}=3.5 \times 10^{17}$	V=2500
P=760	$d=1.316 \times 10^{-4}$	$n^{s,0}=7.6 \times 10^{17}$	V=2500

The goal of this test was to compare these different conditions for various times, and report the resultant charge and energy densities; as well as the relative dynamics of

the system. During a discussion with Bailey (1) it was discovered that using a transformation of parameters approach, it was possible to fully describe the results of the simulation, for any combination of the characteristic parameters listed above, given a solution under any other conditions. This would have been advantageous when comparing any previously published results, as well as analytic solutions if available. However, as seen in the figures below, unstable behavior was observed. The charge densities of the $P = 100$ Torr and greater cases completely disappeared during the first microsecond of operation. For simulation run times on the order of nanoseconds, unpredictable instabilities at these higher pressures were observed, but not reported on here. These instabilities were thought to arise from the values returned by the electron energy equation solution. These energy density values exhibited extreme oscillatory behavior, and negative values were sometimes generated. The location of the problems appeared to occur at the boundaries of the system, but was found to occur at other locations as well for longer run times. Therefore, the boundary conditions of the system were determined to not be the cause of the instability. A good deal of work went into isolating the problems with the energy equation; but it was eventually eliminated from the program, and replaced by another method for determining the local rate and transport values as discussed in the next section.

In Fig 31 below, it is seen that the electron density behaves as discussed in the DC discharge sheath section for the 10 Torr case near the electrodes; but exhibits instabilities which eventually return to a steady state value, in the central portion of the discharge as seen in Fig 32 and Fig 33. An initial build-up of electrons near the anode in

the 1 Torr case in Fig 31, not present at later times, is seen and gives suspicion of an underlying numeric error. The results in Fig 31 look to be very similar to a steady state solution during the first microsecond of operation, and should have been investigated for earlier times. A magnified view (Fig 33) over various times for the instabilities shown in Fig 32 is presented.

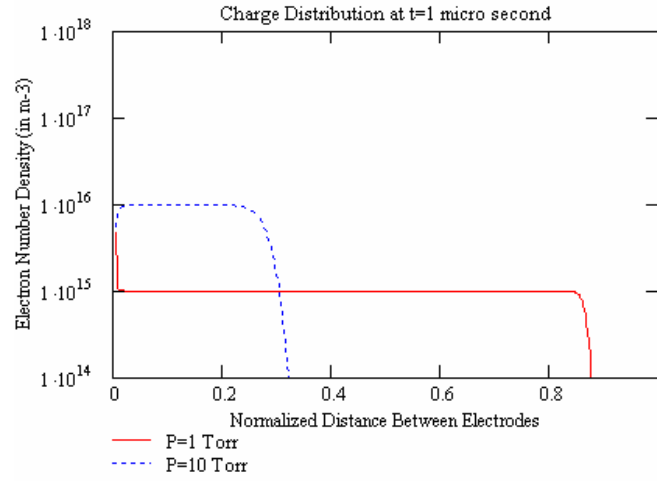


Figure 31. Charge distribution after 1 μs for constant characteristics comparison.

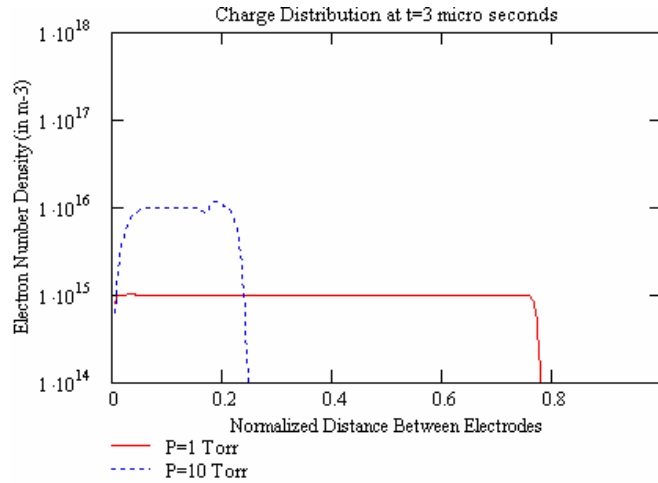


Figure 32. Charge distribution after 3 μs for constant characteristics comparison.

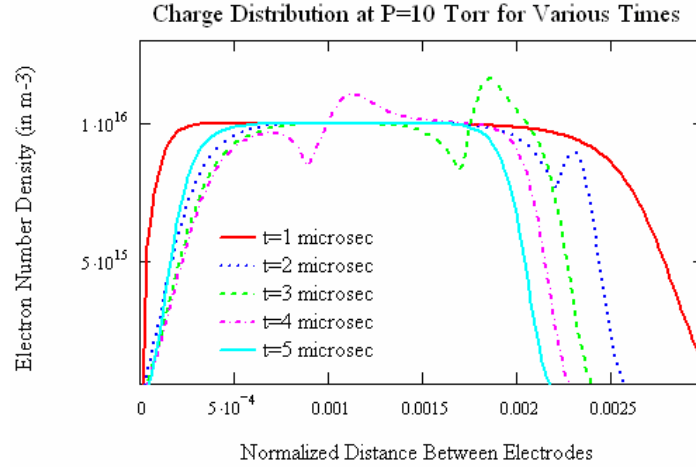


Figure 33. Magnified view of the instabilities near the anode encountered at P=10 Torr.

1D Fixes

Eventually, the erratic behavior of the numeric code was linked to the values of the local average electron energy which are used to determine the rate and transport coefficients as previously described. The setting of minimum and maximum values of these energies in an attempt to keep the results within the range of *goodness* for the fits, masked a problem with the solution of the energy equation. Negative numbers, which began appearing at the boundaries and sometimes at apparently random locations throughout the computational domain, created serious problems for the numeric code. Therefore the energy equation was eliminated, and replaced by the reduced field representation for determining the rate and transport coefficients. This reduced field representation, previously defined as:

$$\text{Reduced Field} = \frac{\vec{E}}{N_{Neutral}},$$

is a characteristic of the conditions in the plasma, and is related to the local average electron energy. Instead of having to rewrite the rate and transport coefficient fit portion of the numeric code, the BOLSIG solver was once again used to relate the reduced field to the average local electron energy as seen below. A fit of this relationship was determined, and used in conjunction with the previous fits to assign new coefficients to all points in the system as seen in Fig 34 below. This approach also had difficulties associated with it, and the range over which the coefficients could be accurately described was further reduced because of the *goodness* of the fits. This limited the range of input parameters, such as electrode potential values and pressures to a specific range. Unfortunately, this range did not include the specified parameter values for the constant characteristics comparison test discussed above. The initial guess of 3.0 eV for the average electron energy for this test case reported above was found to be in error, and was most likely the main contributor to the erratic behavior observed. This value did not allow for accurate initial rate and transport coefficients and limited the ability of the simulation to produce self sustaining ionization. The correct value for the initial average local electron energy value should have been approximately 13 eV, as estimated using the reduced field characteristic. This energy value is well outside the range for which the rate and transport fits were calculated, and presents a significant limitation to the suitability of this numeric code for modeling realistic systems. Unfortunately, this oversight was not found until very late in the project, and time constraints did not allow for it to be corrected. New BOLSIG fits over a wider range of electron energies or direct reduced field value fits introduced into the code may take care of this limitation in the future.

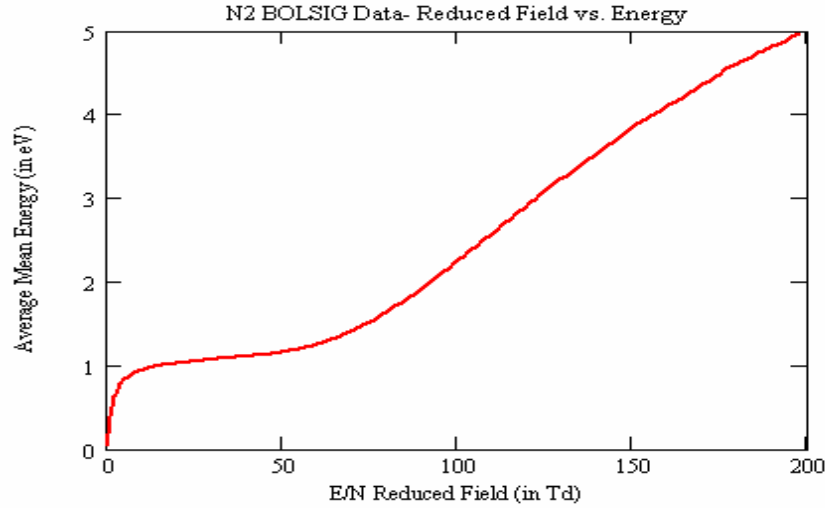


Figure 34. BOLSIG fits for relating the reduced field to the local average electron energy.

With the electron energy equation eliminated and the conditions under which the code could be run more definitively specified, it was found that the source of the negative energy values was actually from the solution of the electron continuity equation. Under certain time step and computational cell spacing conditions, it was found that the solution to the governing equations, especially the electron continuity equation, gave inaccurate results at the boundaries because of the interaction of the thermal velocity used to describe the boundary flux, and the local field and mobility coefficient. Special care had to be taken to not let the rate at which the electrons moved through the system, exceed what the spatial discretization of the model could accurately handle. This was done by carefully choosing the distance between cells and the time step. By using the expected thermal velocities of the electrons under the conditions tested, the cell spacing was adjusted so that the electrons were not allowed to move more than $\frac{1}{4}$ of a cell during each time step. As seen in Eq (56) below (which is Eq (18) rewritten for clarity) the method used to solve the governing equations, could potentially overstep its bounds, leading to an

erroneous negative result for the new time. This occurred when the field driven flux and the thermal flux were oppositely directed.

$$n_{adjacent}^{s,t} = \left(\vec{\Gamma}_{Scharfetter-Gummel}^{s,t} + \vec{\Gamma}_{thermal}^{s,t} + S - L \right) \frac{\Delta t}{\Delta x} + n_{adjacent}^{s,t-1} \quad (56)$$

Various instabilities were still found after all these fixes had been implemented, and no correlation between when or where they would present themselves was found. This made it difficult to focus in on any other areas to fix problems. No further 1D results were obtained.

2D Results and Problems

The 1D and 2D codes were developed simultaneously, and therefore problems found in one had to be addressed in the other. Obtaining even preliminary results from the 2D code proved difficult because of a lack of suitable initial conditions. The plan was to introduce a Gaussian distribution of charge as seen in Fig 35 below, disallow any charge buildup on the dielectric surface, and run the simulation until a steady state solution was reached. The exposed driven electrode can be seen towards the bottom left of the domain, while the grounded electrode is buried in the dielectric material. The peak charge density seen below is about 10^{15} m^{-3} , which falls off rapidly to zero in the outer regions of the computational area.

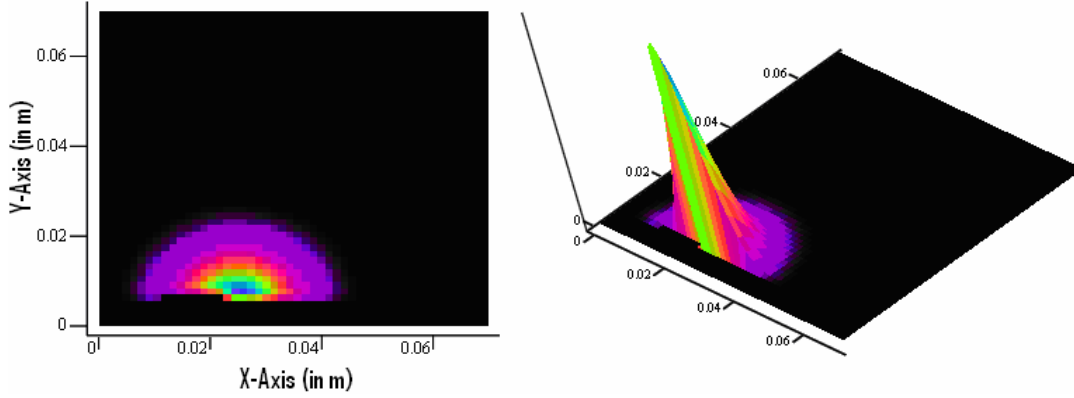


Figure 35. Gaussian used as an initial condition for charge density distribution.

Due to the previously described difficulties and problems finding erratically behaving cells in the much larger 2D geometry, the convergence criteria was never met, and therefore no suitable initial conditions could be implemented. Definite changes in the density profile, charge accumulation, and evolution of the potential profile over time were observed and looked nominally like one would expect, as seen below. Here the dimensions of the 2D system reflect a physically realistic set-up, with the base of the computational area grounded, the driven electrode in the bottom left of the region is held at 2.5kV, and the grounded electrode is towards the bottom right. Rate and transport coefficients are determined using the reduced field representation fix from the 1D environment, and the initial density distribution is the Gaussian from Fig 35 above. The 100% N_2 background gas pressure is 1 Torr, and the driven electrode is exposed. Secondary emission of electrons due to electrode impact by ions is turned on, but not expected for this configuration since the driven electrode is held at a positive potential. The contour lines for the resultant potential profile over time are shown in Fig 36, as well as the evolution from the initial Gaussian distribution of the electron number density in

Fig 37. Notice the erratic behavior of the density on the left side of the computational region around the driven electrode in Fig 37. A suitable explanation for this behavior was not found. Also notice the charge buildup on the dielectric surface in Fig 38. It progressed from an initial condition of zero everywhere, and shows the greatest buildup in regions closest to the electrodes. Overlaid is the representative initial electron density distribution at the points directly above the dielectric surface. The shape of which seems to correspond to the calculated charge accumulation, but notice the erratic behavior of the charge density to the left of the electrode. The value of the reported charge accumulation points can be estimated by considering the initial conditions of the electron thermal velocity, the boundary conditions, and the electron number density. This estimate showed good agreement to the calculated value, so the charge accumulation was considered in line with what should be expected. The charge buildup is thought to migrate down the length of the buried electrode as time progresses, and can narrowly be seen upon close inspection and interpretation of the potential profile plots in Fig 36 below.

No confidence was placed in these results however because of the difficulties in reaching a steady state solution associated with the 2D code that were encountered. These problems were indicative of either program coding errors or basic physical model assumptions and techniques that need to be worked out before any more work is done.

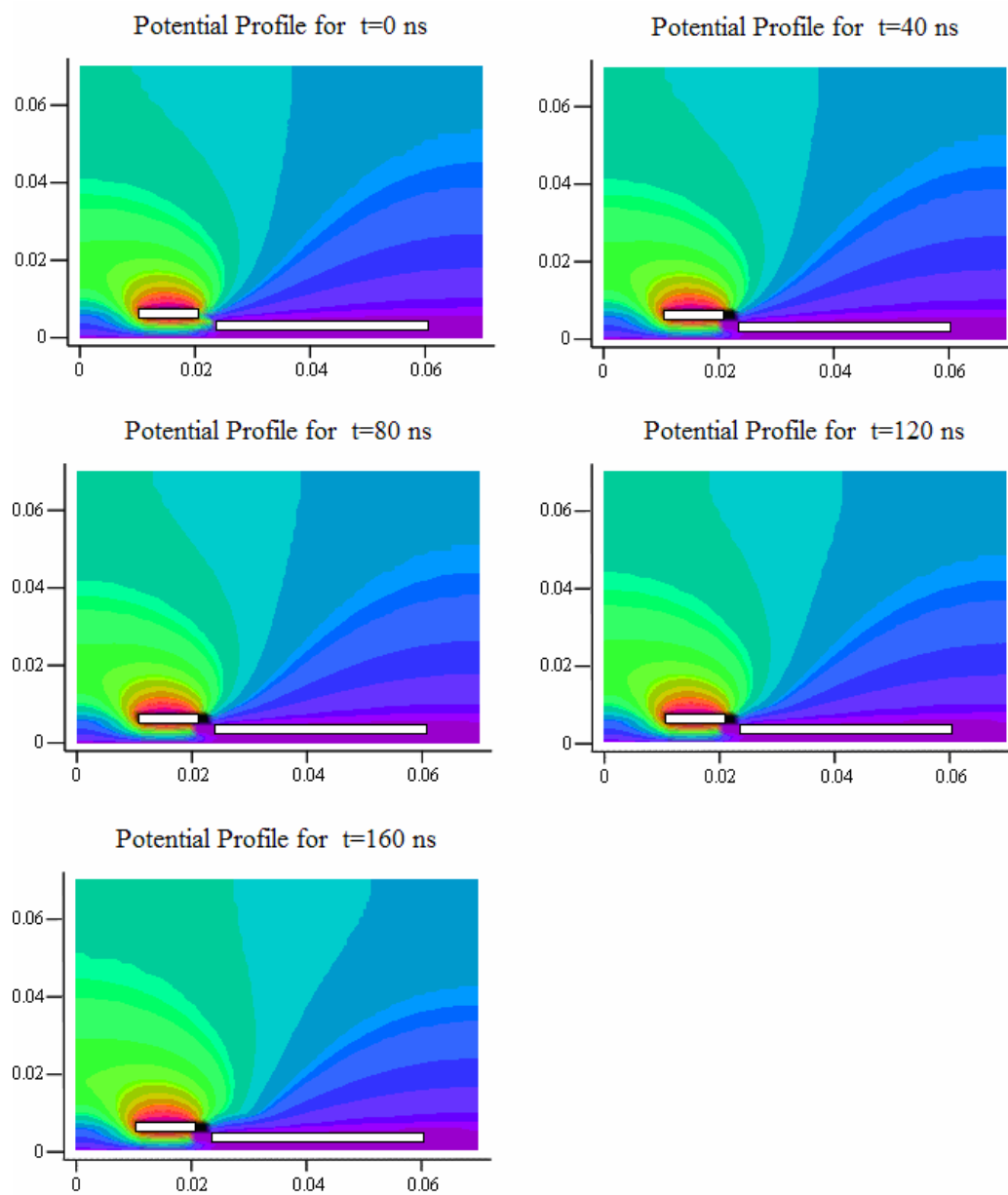


Figure 36. Plots of the 2D potential profile progression for various times. Changes in the profile are seen as charge moves in the system and accumulates on the dielectric surface.

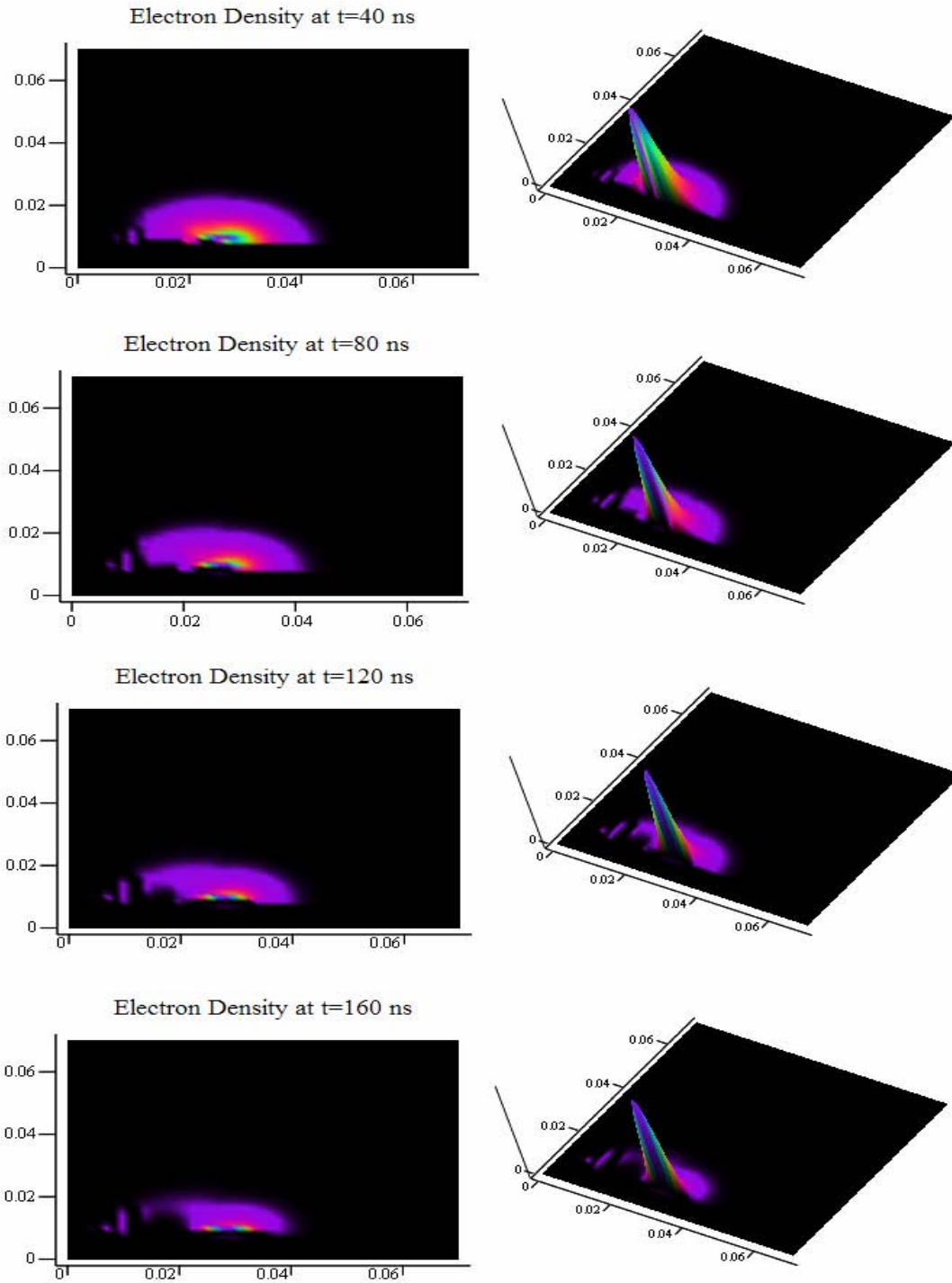


Figure 37. Electron number density for various times after initial Gaussian. Instabilities around the exposed electrode area are seen.

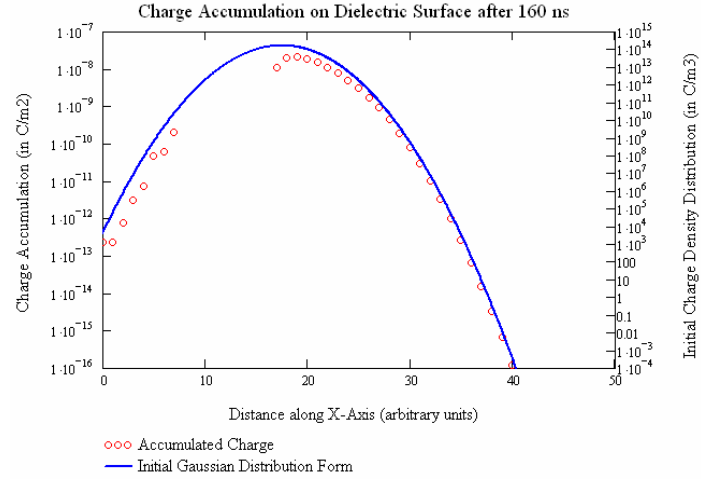


Figure 38. Charge buildup on the dielectric surface at end of simulation. The region between 7 and 17 units on the axis is the location of the exposed electrode. Therefore, no charge was allowed to accumulate there.

V. Summary of Work and Recommendations for Future Efforts

Summary of Work

This project developed three governing equations used to characterize the macroscopic properties of the plasma dynamics of a 1D and 2D plasma actuator set-up. Methods for determining the rate and transport coefficients, solving for the potential profile of the system, and integrating all the pieces into a sequential solving algorithm were presented. Preliminary results were found for the DC discharge sheath model, the ambipolar diffusion case, and by holding some characteristic parameters of the system constant. The main goal of developing an accurate predictor tool, in good agreement to the experimentally observed flow control and boundary layer reattachment forces, for determining the momentum transfer to the neutral air flow of a system by the moving plasma, was not accomplished. However an accurate potential solver in both 1D and 2D was shown and that represents a suitable achievement.

Recommendations for Future Efforts

Various improvements can be implemented to the current code in the future. Changes to the dimensions of the computational area should be made in order to save computational time in regions of low activity, as well as allowing for the simulation of more realistic rectangular like regions, with many electrodes present (as seen from experimental results in Fig 39 below), and a higher resolution view of the progression of the plasma close to the boundary surface. The placement of grounded and driven electrodes should be examined, and allowed to overlap to study if any benefit can be

obtained through this geometry. Grid spacing should be allowed to vary from place to place within the domain, to more accurately model the interfaces and the geometry of the electrodes in the 2D case. Better characterization of the dielectric surface where charge build-up is allowed to either flow through the dielectric material due to the applied field or *jump-off* to contribute to the ionization under reversing field conditions should be looked at. The boundary conditions, and the cause of the instabilities present in the 1D and 2D simulations described above also need more examination.

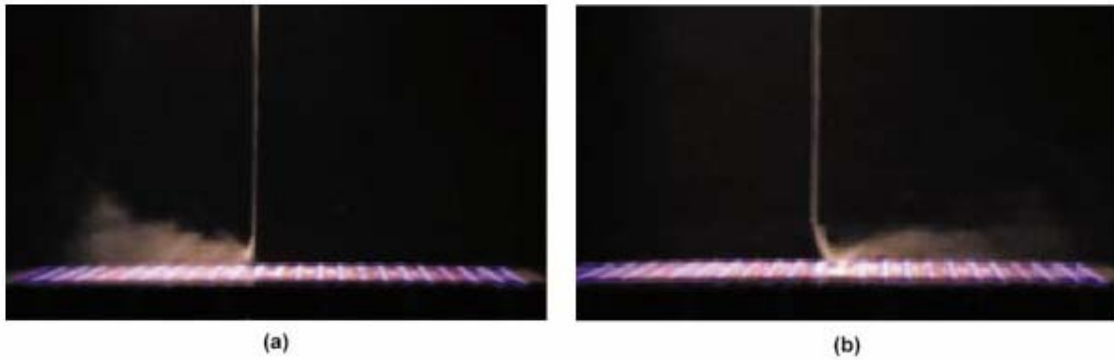


Figure 39. Induction of flow over electrodes with various potentials phasing (17:2125).

The most computationally intensive portion of the program is the potential solver, and it would be very interesting to look at other methods for solving the potential, especially in 2D. By looking at the traditional 5-point method it can be seen that the full matrix for solving the system implicitly has a pentadiagonal like symmetry as seen below in Fig 40. The uppermost and lowermost diagonals vary in their position depending on the size of the array, but the center tridiagonal feature remains. The figure below shows the basic set-up for a 6X6 grid where the bottom row is grounded, and the sides and top are limited by boundary conditions to make the perpendicular component of the electric

field equal to zero. As before, this condition is physically unrealistic, except in cases where the edges are very far away from the electrodes and active region; but serves to keep all charged particles inside the system. No dielectrics or electrodes have been introduced in this set-up. A brief search of numerical matrix techniques did not reveal a unique direct (implicit) method for solving this pentadiagonal matrix. It could however be solved using a computationally intensive Gaussian elimination scheme. It would be interesting to actually compare the time for convergence of the iterative line method used in this project and the time for a solution to the pentadiagonal system using a direct method, or other type of iterative technique.

$$\begin{pmatrix}
 3 & 1 & & & 1 & & & & \\
 1 & 4 & 1 & & & 1 & & & \\
 & 1 & 4 & 1 & & & 1 & & \\
 & & 1 & 3 & 0 & & & 1 & \\
 1 & & & 0 & 3 & 1 & & & 1 \\
 & 1 & & & 1 & 4 & 1 & & 1 \\
 & & 1 & & & 1 & 4 & 1 & 1 \\
 & & & 1 & & 1 & 3 & 0 & 1 \\
 & & & & 1 & & 0 & 3 & 1 & 1 \\
 & & & & & 1 & & 1 & 4 & 1 & 1 \\
 & & & & & & 1 & & 1 & 4 & 1 & 1 \\
 & & & & & & & 1 & & 1 & 3 & 0 & 1 \\
 & & & & & & & & 1 & & 0 & 2 & 1 \\
 & & & & & & & & & 1 & & 1 & 3 & 1 \\
 & & & & & & & & & & 1 & & 1 & 2
 \end{pmatrix}
 \begin{pmatrix}
 \phi_{1,1} \\
 \phi_{1,2} \\
 \phi_{1,3} \\
 \phi_{1,4} \\
 \phi_{2,1} \\
 \phi_{2,2} \\
 \phi_{2,3} \\
 \phi_{2,4} \\
 \phi_{3,1} \\
 \phi_{3,2} \\
 \phi_{3,3} \\
 \phi_{3,4} \\
 \phi_{4,1} \\
 \phi_{4,2} \\
 \phi_{4,3} \\
 \phi_{4,4}
 \end{pmatrix}
 =
 \begin{pmatrix}
 (\rho_{1,1}(\Delta x)^2 / \varepsilon) + gnd \\
 (\rho_{1,2}(\Delta x)^2 / \varepsilon) + gnd \\
 (\rho_{1,3}(\Delta x)^2 / \varepsilon) + gnd \\
 (\rho_{1,4}(\Delta x)^2 / \varepsilon) + gnd \\
 \rho_{2,1}(\Delta x)^2 / \varepsilon \\
 \rho_{2,2}(\Delta x)^2 / \varepsilon \\
 \rho_{2,3}(\Delta x)^2 / \varepsilon \\
 \rho_{2,4}(\Delta x)^2 / \varepsilon \\
 \rho_{3,1}(\Delta x)^2 / \varepsilon \\
 \rho_{3,2}(\Delta x)^2 / \varepsilon \\
 \rho_{3,3}(\Delta x)^2 / \varepsilon \\
 \rho_{3,4}(\Delta x)^2 / \varepsilon \\
 \rho_{4,1}(\Delta x)^2 / \varepsilon \\
 \rho_{4,2}(\Delta x)^2 / \varepsilon \\
 \rho_{4,3}(\Delta x)^2 / \varepsilon \\
 \rho_{4,4}(\Delta x)^2 / \varepsilon
 \end{pmatrix}$$

Figure 40. Pentadiagonal matrix for implicit potential solution.

Given the promise of DBD device technology to radically alter the aviation world of today and the specific benefits associated with its development to the United States Air Force, should compels the aerospace industry and academic community to seriously look at the technology as a way of preserving America's air supremacy in the 21st century.

Bibliography

- 1 Bailey, William. Personal interview. May 2006.
- 2 Boeuf, J.P. and L. C. Pitchford. "Two-dimensional model of a capacitively coupled rf discharge and comparisons with experiments in the Gaseous Electronics Conference reference reactor." *Physical Review E*, 51:1376-1384 (February 1995).
- 3 *BOLSIG+*. Version 1.01, Computer software. Hagelaar, Gerjan. Centre National de la Recherche Scientifique, Toulouse, France, Oct 2005.
- 4 Burden, Richard L. and Faires, J. Douglas. Numerical Analysis 8th Edition. Belmont, California: Thompson Brooks/Cole, 2005.
- 5 Chapra, Steven C. and Canale, Raymond P. Numerical Methods for Engineers 4th Edition New York: McGraw Hill, 2002.
- 6 Cravens, Thomas E., Alexander J. Dessler, John T. Houghton, Michael J. Rycroft. *Physics of Solar System Plasmas*. New York: Cambridge University Press, 1997.
- 7 Enloe, C. L., McLaughlin, T. E., VanDyken, R.D., Kachner, K.D., Jumper, E.J., Corke, T.C., "Mechanisms and Responses of a Single Dielectric Barrier Plasma", AIAA Paper 2003-1021.
- 8 Font, G.I., Jung, S., Enloe, C. L., McLaughlin, T. E., Morgan, W.L., and Baughn, J. W., "Simulation of the Effects of Force and Heat Produced by a Plasma Actuator on Neutral Flow Evolution", AIAA Paper 2006-0167.
- 9 Font, Gabriel I. "Boundary Layer Control with Atmospheric Plasma Discharges." 40th AIAA/ASME/SAE/ASEE Joint Propulsion Conference and Exhibit, Ft. Lauderdale, FL, 11-14 July 2004, paper AIAA 2004-3574.
- 10 Griffiths, David J. Introduction to Electrodynamics 3rd Edition. Upper Saddle River, New Jersey: Prentice Hall, 1999.
- 11 Hagelaar, G.J.M. Modeling of Microdischarges for Display Technology. Technische Universiteit Eindhoven, Eindhoven, The Netherlands, November 2000.
- 12 Hilbun, William M. and Benjamin J. Case. "Preliminary Development of a Computational Model of a Dielectric Barrier Discharge." 49th AIAA Aerospace Sciences Meeting and Exhibit, Reno, NV, 10-13 January 2005, paper AIAA 2005-1176.
- 13 Hilbun, William. "MN Approach to Modeling Plasma Actuators." UF/GERC (Shalimar, FL), 13 May 2004.

- 14 Kogelschatz, U., Eliasson, B., Egli, W., "From ozone generators to flat television screens: history and future potential of dielectric-barrier discharges", Pure Appl. Chem, 71, 1819-1828 (1999).
- 15 Marchand, Krista G. Computational Model of One-Dimensional Dielectric Barrier Discharges. Air Force Institute of Technology, Wright-Patterson AFB, OH, May 2005.
- 16 Poggie, J. and D.V. Gaitonde. "Electrode Boundary Conditions in Magnetogasdynamic Flow Control." 40th Aerospace Sciences Meeting and Exhibit, 14-17 January 2002, Reno, NV, paper AIAA 2002-0199.
- 17 Roth, J. Reece. "Aerodynamic flow acceleration using paraelectric and peristaltic electrohydrodynamic effects of a One Atmosphere Uniform Glow Discharge Plasma." Physics of Plasmas 10:2117-2126 (May 2003).
- 18 Roth, J Reece. And Sherman, Daniel M. "Boundary Layer Flow Control with a One Atmosphere Uniform Glow Discharge Surface Plasma." AIAA paper 98-0328.
- 19 Smithro, Christopher. "Kinetic Theory of Plasmas 650." Course Notes, Air Force Institute of Technology, Wright-Patterson AFB, OH, 26 Apr 2005.
- 20 Unknown, Author. "Overview of DBD Compared to Three Conventional Discharges." Course Notes, shira.iic.kyoto-u.ac.jp/lecture_notes/plasma-process/DBD-Lecture-Note.pdf 24 Jan 2005.

Vita

1st Lieutenant Christopher Charles graduated from Heritage Christian High School of Sharpsburg, GA in 1997. He subsequently attended Northwestern Preparatory School of Crestline, CA, on a Falcon Foundation scholarship, in the winter of 1997 and Clayton College and State University of Morrow, GA in the spring of 1998. Lt Charles was accepted to the United States Air Force Academy (USAFA), Colorado Spring, CO in the summer of 1998.

Upon graduation from USAFA earning a Bachelor of Science degree in Physics (with a focus on Astronomy) and a minor in Mathematics in 2002, Lt Charles was placed on casual status, waiting pilot training, at the 452nd Flight Test Squadron, Edwards AFB, CA. He was reassigned to the Air Force Research Laboratory, Propulsion Directorate, Spacecraft Propulsion Division, Edwards AFB, CA.

In the summer of 2004, Lt Charles was enrolled at the Air Force Institute of Technology, Wright-Patterson AFB, OH in the Applied Physics curriculum. After graduation, Lt Charles will be assigned to the Air Force Research Laboratory, Wright-Patterson AFB, OH, working at the Materials Laboratory, Laser Hardened Materials Branch.

REPORT DOCUMENTATION PAGE				Form Approved OMB No. 074-0188	
<p>The public reporting burden for this collection of information is estimated to average 1 hour per response, including the time for reviewing instructions, searching existing data sources, gathering and maintaining the data needed, and completing and reviewing the collection of information. Send comments regarding this burden estimate or any other aspect of the collection of information, including suggestions for reducing this burden to Department of Defense, Washington Headquarters Services, Directorate for Information Operations and Reports (0704-0188), 1215 Jefferson Davis Highway, Suite 1204, Arlington, VA 22202-4302. Respondents should be aware that notwithstanding any other provision of law, no person shall be subject to a penalty for failing to comply with a collection of information if it does not display a currently valid OMB control number.</p> <p>PLEASE DO NOT RETURN YOUR FORM TO THE ABOVE ADDRESS.</p>					
1. REPORT DATE (DD-MM-YYYY) 14-05-2006		2. REPORT TYPE Master's Thesis		3. DATES COVERED (From – To) Sept 2005 – May 2006	
4. TITLE AND SUBTITLE COMPUTATIONAL MODELING OF THE DIELECTRIC BARRIER DISCHARGE (DBD) DEVICE FOR AERONAUTICAL APPLICATIONS				5a. CONTRACT NUMBER	
				5b. GRANT NUMBER	
				5c. PROGRAM ELEMENT NUMBER	
6. AUTHOR(S) Charles, Christopher S., 1 st Lieutenant, USAF				5d. PROJECT NUMBER	
				5e. TASK NUMBER	
				5f. WORK UNIT NUMBER	
7. PERFORMING ORGANIZATION NAMES(S) AND ADDRESS(S) Air Force Institute of Technology Graduate School of Engineering and Management (AFIT/EN) 2950 Hobson Way WPAFB OH 45433-7765				8. PERFORMING ORGANIZATION REPORT NUMBER AFIT/GAP/ENP/06-02	
9. SPONSORING/MONITORING AGENCY NAME(S) AND ADDRESS(ES) N/A				10. SPONSOR/MONITOR'S ACRONYM(S)	
				11. SPONSOR/MONITOR'S REPORT NUMBER(S)	
12. DISTRIBUTION/AVAILABILITY STATEMENT APPROVED FOR PUBLIC RELEASE; DISTRIBUTION UNLIMITED					
13. SUPPLEMENTARY NOTES					
14. ABSTRACT This thesis explores the numerical simulation of the Dielectric Barrier Discharge device in both a 1D and 2D environment. Using fluid equation techniques, computational results for various conditions and geometries are explored. Results are compared to analytic or experimental data whenever possible. Solutions to Poisson's equation for the potential, electron and ion continuity equations, and the electron energy equation are solved semi-implicitly in a sequential manner, using the computationally efficient Thomas algorithm. The Scharfetter-Gummel flux discretization method is used to add stability to the code. Rate and transport coefficients are calculated as a function of the local average electron energy. The 2D geometry includes a Gauss-Seidel line iterative method to solve Poisson's equation, and a superposition method for keeping track of ion, electron, and electron energy fluxes. Conditions are implemented to close the computational region at the boundaries, and to account any space or surface charge. Results from the 1D and 2D code are shown, as well as limitations of the current work and proposed future refinements.					
15. SUBJECT TERMS Dielectric Barrier Discharge, DBD, Flow-control, Numerical Fluid Approach, Computational Plasma Dynamics					
16. SECURITY CLASSIFICATION OF:			17. LIMITATION OF ABSTRACT UU	18. NUMBER OF PAGES 84	19a. NAME OF RESPONSIBLE PERSON Dr. William F. Bailey
a. REPORT U	b. ABSTRACT U	c. THIS PAGE U			19b. TELEPHONE NUMBER (Include area code) (937) 785-3636, ext 4501 (William.Bailey@afit.edu)